Chapter 14
Inorganic-Organic Hybrid Materials Based on Nanopolyoxometalates

Yitong Wang and Jingcheng Hao

Abstract Various types of nano-scale polyoxometalates (POMs) with beautiful topologies has been synthesized successfully by destroying the hydration shell of the anions caused by the extremely hydrophilic surface. Their magnetic, electronic, and photoluminescent properties and valuable applications in catalysis, medicine, and material science are discussed. Meanwhile, the last ten years have witnessed a remarkable development in terms of preformed organic-inorganic POM-based hybrid systems for the rational design of functional architectures, assemblies and materials. Hydrophilic POMs of different sizes and shapes can interact with hydrophobic cationic surfactants, the resulting materials show amphiphilic properties with electrostatic interactions between the hydrophilic and hydrophobic components, called Surfactant-Encapsulated Clusters (SECs) or Surfactant-Encapsulated-POMs (SEPs). This hydrophobic surfactant-encapsulated clusters (HSECs) can fabricated through covalent or non-covalent interaction, which can construct ordered self-assembly, e.g. robust onionlike structures, honeycomb films or giant vesicle. Moreover, This ordered giant vesicle acts as building block to fabricate three dimensional structures. In addition, SECs can further self-assemble to give a variety of nanostructures on various surfaces/interfaces, among them, the most representative nanostructures discussed below is ordered honeycomb films, which is carried out by a simple solvent-evaporation method. It is reasonable to assume that the condensed water microdroplets induced by the quick evaporation of solvents play an important role as template for the formation of pores. Various factors are being investigated to construct thin films with different morphologies. We hope the inorganic-organic hybrid functional materials based on POMs will bridge polyoxometalate chemistry and material chemistry, which can be further explored application in many fields.

Keywords Polyoxometalates · Surfactant · Self-assembly · Inorganic-organic hybrids · Porous films

Y. Wang · J. Hao (✉)
Key Laboratory for Colloid and Interface Chemistry,
Ministry of Education, Shandong University, Jinan 250100, China
e-mail: jhao@sdu.edu.cn

J. Li (ed.), *Supramolecular Chemistry of Biomimetic Systems*,
DOI 10.1007/978-981-10-6059-5_14

14.1 Introduction to Developed POMs

Polyoxometalates (POMs) chemistry has been known for two centuries, which has received tremendous impetus from the intensive review by Pope and Müller in 1991 [1] and has accordingly achieved considerable progress in the last two decades. Metal-oxygen cluster-anions (polyoxometalates, or POMs) are discrete, anionic metal-oxide clusters of early transition metals [2, 3]. Composed principally of Mo, W, V and Nb, they represent a large and important class of inorganic molecules and materials, whose relevance is being highlighted in a number of review articles [4–6], with diverse range of dynamic molecular structures, a wide range of physical and chemical properties, and large domains of applications [7–11].

In the last three decades, various polyoxometalates have been synthesized successfully by destroying the hydration shell of the anions caused by the extremely hydrophilic surface [12–14]. Meanwhile, the last ten years have witnessed a remarkable development in terms of preformed organic-inorganic POM-based hybrid systems for the rational design of functional architectures, assemblies and materials [15–18].

14.1.1 Structures of POMs

Polyoxometalate structures are based on $\{MO_x\}$ polyhedra sharing vertices, edges, or more rarely, faces. In general, the typical structures of polyoxoanions are Keggin-type [19], Dawson-type [20], Waugh-type [21], Anderson-type [22], Silverton-type [23] and Lindquist-type [24], as shown in Fig. 14.1 and the Keggin-type and the Dawson-type are the most common type. In addition, POMs reveal a huge variety of shapes, sizes and compositions, such as, a "Keplerate-type" sphere $\{Mo_{132}\}$ $(NH_4)_{42}$ $\left[\left\{\left(Mo^{VI}\right)Mo_5^{VI}O^{21}(H_2O)_6\right\}_{12}\right.$ $\left.\{Mo_2O_4(CH_3COOH)\}_{30}\right]\cdot ca\cdot 300H_2O\cdot ca\cdot 10CH_3COONH_4$ and $\{Mo_{72}Fe_{30}\}$ $[Mo_{72}^{VI}Fe_{30}^{III}O_{252}(CH_3COO)_{12}\{Mo_2O_7(H_2O)\}_2\{H_2Mo_2O_8(H_2O)\}(H_2O)_{91}]\cdot ca\cdot 150H_2O$, a "giant wheel-type" cluster $\{Mo_{154}\}$ $Na_{15}[Mo_{154}O_{462}H_{14}(H_2O)_{70}]_{0.5}[Mo_{152}O_{457}H_{14}(H_2O)_{68}]_{0.5}\cdot ca\cdot 400H_2O$, a "protein-sized blue lemon" $\{Mo_{368}\}$ $(Na_{48}$ $[H_{496}Mo_{368}O_{1464}S_{48}]$ $\cdot ca\cdot 1000$ $H_2O)$ [25], and sandwich-type clusters, $\{Mn_2Bi_2W_{20}\}$ $(Na_6(NH_4[(Mn(H_2O)_3(WO)_2(BiW_9O_{33})_2])$ [26] and $\{EuW_{10}\}$ $(Na_9[EuW_{10}O_{36}]\cdot 32H_20)$ [27]. Compared with the traditional salts, POMs are formed by linking metal oxide polyhedra which are composed of many more atoms (even thousands), and become giant, with diameters of several nanometers. The different colors of the POMs in Table 14.1 represent different types of metal oxide polyhedral: light blue, MoO_7 pentagon bi-pyramid polyhedron; dark blue, MoO_6 octahedron; yellow, FeO_6 octahedron; light green, CrO_6 octahedron; dark green, VO_6 octahedron, which enable researchers to construct POMs with different topologies and sizes [11]. Due to the excess of oxo-ligands over metal ions, POMs are usually highly negatively charged, i.e., macro-polyoxoanions with high solubility in water and polar solvents exhibit unique solution behaviors. In dilute solutions,

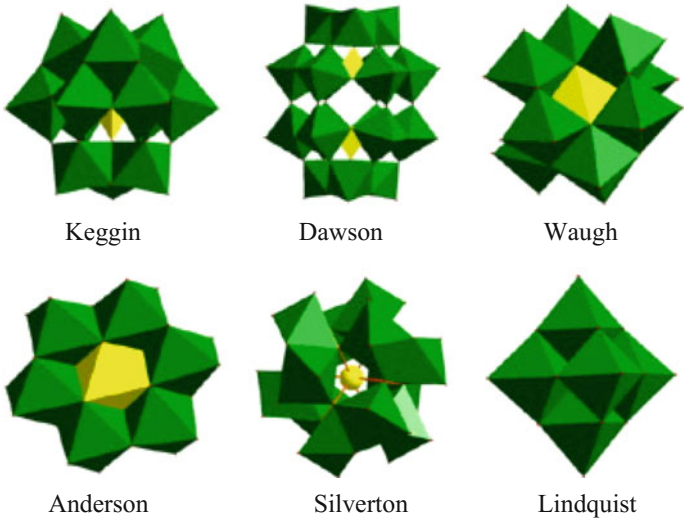

Fig. 14.1 Six typical structures of polyoxometalates

Table 14.1 Information on the structure, charge density, and self-assembly behavior of some typical giant polyoxometalate molecular clusters

Polyoxoanion	$\{Mo_{72}Fe_{30}\}$			$\{Mo_{72}Cr_{30}\}$	$\{Mo_{154}\}$	$\{Cu_{20}P_8W_{48}\}$	$\{P_4Y_9W_{43}\}$	$\{Mo_{132}\}$	$\{Mo_{72}V_{30}\}$
Molecular structure									
Negative charge	0-1	1-29		5	15	25	30	42	31
Size (nm)		2.5		2.5	3.6×1.2	2.2×1.1	4.0×2.0×2.0	2.9	2.5
Charge density (nm^{-2})	0-0.051 (pH < 2.9)	0.015-1.477 (2.9 < pH < 6.6)	Unstable (pH > 6.6)	0.255	0.543	1.291	1.08	1.590	1.579
Self-assembly in aqueous solution	No	Yes	No	Yes	Yes	Yes	Yes	Yes at high conc.	No
R_h of Blackberry (nm)	48-15			60	45	38	46		

Formula	References
$\{Mo_{72}Fe_{30}\}\left[Mo_{72}^{VI}Fe_{30}^{III}O_{252}(CH_3COO)_{12}\{Mo_2O_7(H_2O)\}_2\{H_2Mo_2O_8(H_2O)\}(H_2O)_{91}\right]\cdot ca\cdot 150H_2O$	[30]
$\{Mo_{72}Cr_{30}\}\left[\{Na(H_2O)_{12}\}\{Mo_{72}^{VI}Cr_{30}^{III}O_{252}(CH_3COO)_{19}(H_2O)_{94}\}\right]\cdot ca\cdot 120H_2O$	[34]
$\{Mo_{154}\}\ Na_{15}[Mo_{154}O_{462}H_{14}(H_2O)_{70}]_{0.5}[Mo_{152}O_{457}H_{14}(H_2O)_{68}]0.5\cdot ca\cdot 400H_2O$	[28]
$\{Cu_{20}P_8W_{48}\}\ K_{12}Li_{13}[Cu_{20}Cl(OH)_{24}(H_2O)_{12}(P_8W_{48}O_{184})]22H_2O$	[33]
$\{P_4Y_9W_{43}\}\ K_{15}Na_6(H_3O)_9[(PY_2W_{10}O_{38})_4(W_3O_{14})]39H_2O$	[32]
$\{Mo_{132}\}\ (NH_4)_{42}\left[\{(Mo^{VI})Mo_5^{VI}O^{21}(H_2O)_6\}_{12}\{Mo_2O_4(CH_3COOH)\}_{30}\right]\cdot ca\cdot 300H_2O\cdot ca\cdot 10CH_3COONH_4$	[29]
$\{Mo_{72}V_{30}\}Na_8K_{14}(VO)_2[\{(Mo^{VI})Mo_5^{VI}O_{21}(H_2O)_3\}_{10}\{(Mo^{VI})Mo_5^{VI}O_{21}(H_2O)_3(SO_4)\}_2\{V^{IV}O(H_2O)\}_{20}\{V^{IV}O\}_{10}(\{KSO_4\}_5)_2]\cdot ca\cdot 150H_2O$	[31]

macroions behave significantly different from small simple ions (Debye-Hückel theory) because they cannot be treated as point charges or colloidal suspensions (DLVO theory). The size discrepancy between the polyoxoanions and their counter-ions results in the formation of single-layered, hollow, spherical, blackberry structures.

There are two generic families of POMs and some general features are shown in Table 14.1. One is the isopolycompounds (also called isopolyanions or isopolyoxometalates) that contain only the d^0 metal cations and oxide anions, such as $\{Mo_{154}\}$ and $\{Mo_{132}\}$. The other is the heteropoly compounds (also called heteropolyanions or heteropolyoxometalates) that contain one or more p-, d-, or f-block "heteroatorns" in addition to other ions, such as $\{Mo_{72}Fe_{30}\}$, $\{Cu_{20}P_8W_{48}\}$ and $\{P_4Y_9W_{43}\}$. Over half of the elements in the periodic table are known to function as heteroatoms in heteropoly compounds. These heteroatoms can reside either buried in (not solvent accessible) or at surface (solvent accessible) positions in the POM structures.

14.1.2 Properties of POMs

Polyoxometalates are composed of traditional metals and coordinated oxygen atoms. Due to the active outer shell electron of traditional metals, polyoxometalates show excellent electronic versatility. Many researches have demonstrated nano-scale POM clusters are versatile, including electrochemical properties, magnetic properties and photoluminescent properities.

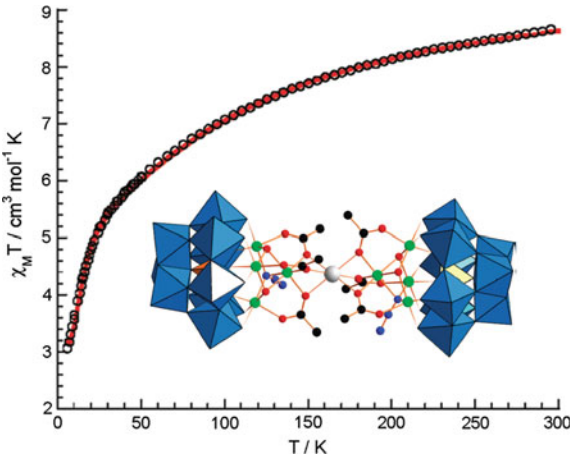

Fig. 14.2 Thermal dependence of $\chi_M T$ for $\{Ni_4SiW_9\}$. The *solid line* represents the best-fit parameters using Hamiltonian. The inset schematically shows polyhedral and ball-and-stick representation of $\{Ni_4SiW_9\}$. Color code: *blue octahedra*, $\{WO_6\}$; *orange tetrahedra*, $\{SiO_4\}$; *green spheres*, Ni; *gray sphere*, Na; *red spheres*, O; *blue spheres*, N; *black sphere*, C. Reprinted with the permission from Ref. [35]. Copyright 2008, American Chemical Society

Pichon et al. discovered and characterized that the high-nuclearity Ni^{II}-substituted polyoxometalate $\{Ni_4SiW_9\}$ ($Na_{15}[Na\{(A\text{-}\alpha\text{-}SiW_9O_{34})Ni_4(CH_3COO)_3(OH)_3\}_2{\cdot}4NaCl{\cdot}36H_2O$) possesses ferromagnetic and antiferromagnetic interactions among clusters concomitantly [35]. As shown in Fig. 14.2, the $\chi_M T$ product continuously decreases from 300 K ($\chi_M T = 8.65\ cm^3\ mol^{-1}\ K$, with the $\chi_M T$ value calculated for eight non-interacting Ni^{II} centers being $8.82\ cm^3\ mol^{-1}\ K$, assuming g = 2.1) to 2 K ($\chi_M T = 2.72\ cm^3\ mol^{-1}\ K$), indicating that antiferromagnetic exchange interactions are predominant in the $\{Ni_4SiW_9\}$. In addition, it has been proved that the Keplerate-type $\{Mo_{72}Fe_{30}\}$ possesses paramagnetism, which were also investigated by experimental investigation and theoretical simulation with the classical and quantum Heisenberg model [36].

The composition of the metal and the shape of the framework define the properties of a POM. Due to the traditional metals, POMs possess rich electrochemical properties [37–40]. For example, in order to study the electrochemical properties of POMs, the wheel-shaped Cu_{20}-tungstophosphate $K_{12}Li_{13}[Cu_{20}Cl(OH)_{24}(H_2O)_{12}(P_8W_{48}O_{184})]22H_2O$ was selected by measuring cyclic voltammetry and controlled potential coulometry in pH = 0 and pH = 5 media [38]. Figure 14.3a shows the cyclic voltammogram (CV) of $Cu_{20}P_8W_{48}$ in a pH = 0 medium. A large current intensity composite reduction wave is observed with its main peak located at 0.113 V, followed by small, hardly distinguishable waves. On potential reversal, small waves are also seen, followed by a large current reoxidation wave located at +0.034 V. This last wave displays the characteristic shape usually encountered for the reoxidation of deposited Cu^0 on electrode surface. Figure 14.3b shows the CV of $Cu_{20}P_8W_{48}$ in a pH = 5 medium. The pattern is composed of two closely spaced reduction waves and well-separated from another set of two closely spaced waves. The authors presumed the first two reduction waves were the two-step reduction of Cu^{2+} to Cu^0 through Cu^+. The two waves featuring the Cu^{2+}/Cu^+ and Cu^+/Cu^0 reduction steps are located at −0.162 and −0.252 V, respectively, and are far from the W^{VI} reduction waves which appear at −0.682 and −0.796 V. It can be conclude that the influence of pH is reflected in the overall negative potential shift of the CV when the medium acidity decreases and W^{VI} reduction waves have much better separation from Cu^{2+} waves at pH = 5 than at pH = 0. The activity in the reduction of nitrate and the intermediate or final products of the polyanion $Cu_{20}P_8W_{48}$ was tested at pH = 0 and pH = 5. However, the waves only can be observed at pH = 5, as shown in Fig. 14.3c, d, a medium in which heteropolyacid-based catalysts are more difficult to obtain than in more acidic solutions. It must be concluded that an efficient catalysis of the reduction of nitrite can be achieved during the reduction of $Cu_{20}P_8W_{48}$.

Moreover, some lanthanide-containing and transition metal-containing polyoxometalates are photoluminescent. For example, a Eu-containing $Na_9[EuW_{10}O_{36}]32H_2O$ [27] polyoxometalates is strongly luminescent under UV light excitation (Fig. 14.4).

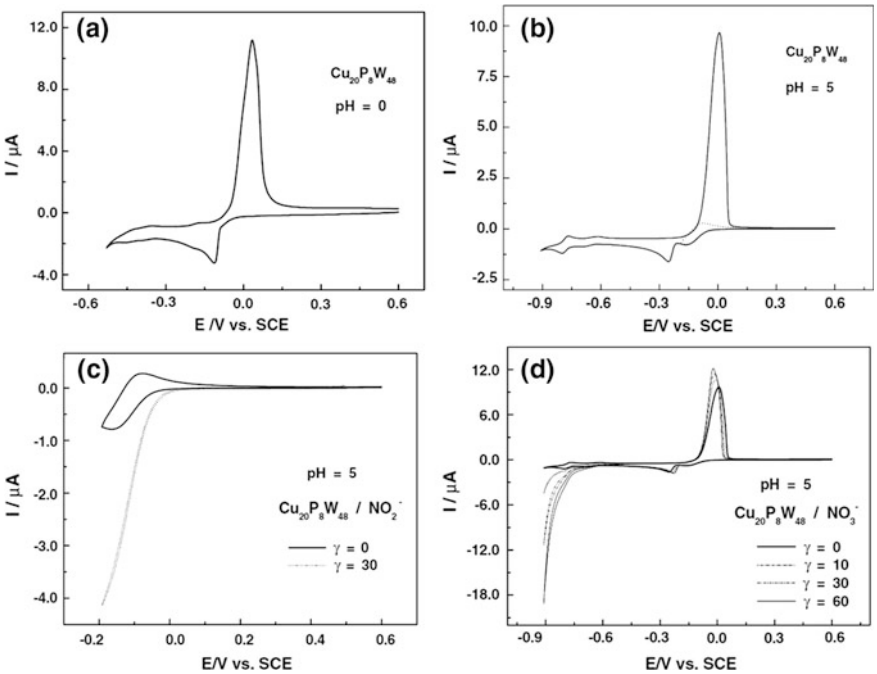

Fig. 14.3 **a** Cyclic voltammograms of 4×10^{-5} M solutions of $Cu_{20}P_8W_{48}$ in H_2SO_4 (pH = 0) medium. The scan rate was 2 mV s^{-1}, the working electrode was glassy carbon (3 mm diameter disc), and the reference electrode was SCE. **b** Cyclic voltammograms of 4×10^{-5} M solutions of $Cu_{20}P_8W_{48}$ in 1 M CH_3COOLi + CH_3COOH (pH = 5) medium. The scan rate was 2 mV s^{-1}, the working electrode was glassy carbon (3 mm diameter disc), and the reference electrode was SCE. **c** Cyclic voltammograms (scan rate: 2 mV s^{-1}) for the electrocatalytic reduction of nitrate with a 4×10^{-5} M solution of $Cu_{20}P_8W_{48}$ in a pH = 5 medium (1 M CH_3COOLi + CH_3COOH). **d** Cyclic voltammograms (scan rate: 2 mV s^{-1}) for the electrocatalytic reduction of nitrite with a 4×10^{-5} M solution of $Cu_{20}P_8W_{48}$ in a pH = 5 medium (1 M CH_3COOLi + CH_3COOH). The excess parameter defined as $\gamma = C^0 (NO_x)/C^0 (Cu_{20}P_8W_{48})$. Reprinted from Ref. [38], Copyright 2012, with permission from Elsevier

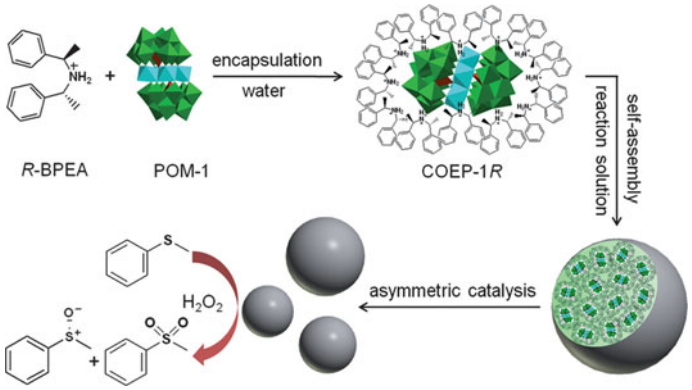

Fig. 14.4 Schematic illustration of the preparation procedure of COEP-1*R* assemblies and their asymmetric catalytic oxidation for methylphenyl sulfide with H_2O_2 (30%). Reproduced from Ref. [45] by permission of the Royal Society of Chemistry

14.1.3 Applications of POMs

Because of their remarkable properties, POMs have a great deal of potential to meet contemporary societal demands regarding health, environment, energy and information technologies, and broad applications as catalysts, photo-electronic/magnetic materials, and biologically active materials. Recently, the researches of polyoxometalates are focused on the development of novel POM-based molecular and composite materials for various applications. POMs hybrid materials can be classified into two categories, which are defined according to the interactions between the hybrid materials and POMs moieties, namely, non-covalent and covalent interactions, respectively. Non-covalently substituted POMs can be assembled through electrostatic interactions, hydrogen bonding, and/or van der Waals interactions [41–44]. Covalent functionalization by grafting organic moieties onto POMs result in the formation of another hybrids. It is also worth noting that covalently substituted POMs still have the capacity for further self-assembly via a variety of interactions, providing an opportunity to construct various interesting supramolecular assemblies. Modifications of POM clusters can enhance the original functionalities, which may lead to hybrid materials with not only value-adding properties, but also synergistic effects.

Due to their specific redox and acidic properties, POMs, as a type of commonly effective catalyst, have been applied for numerous organic transformations. Wu et al. [45] developed chiral polyoxometalate complexes which can be used as microreactors, and exhibited an efficient asymmetric catalytic activity for the oxidation of sulfide with up to 72% enantiomeric excess. The authors used a chiral organic cation to encapsulate POM with high catalytic activity through electrostatic interaction, resulting in the formation of a chiral organic cation-encapsulated POM (COEP) complex. They successfully constructed COEP-based spherical self-assembly complexes in the reaction solutions (Fig. 14.4). The synergistic effect of the two components predominates the catalytic process, in which the POM contributes to the catalysis of sulfoxidation and the chiral organic part provides a chiral microenvironment.

The polyanionic feature of POMs allows them to form complexes with many proteins or peptides containing cationic residues through ionic bonds, thus resulting in potential biological applications [46–50]. Alzheimer's disease (AD) is the most common form of dementia, which is characterized by cerebral extracellular amyloid plaques and intracellular neurofibrillary tangles [51]. Although the molecular mechanisms of AD pathogenesis are not clearly understood owing to its complexity, many efforts have been made to development of Ab inhibitors [52]. Qu's group has demonstrated that the POMs with Wells-Dawson or a Keggin structure showed moderate to high inhibition of Ab aggregation [47, 53]. Furthermore, they developed some POMs/peptides hybrid platforms as the inhibitors of the aggregation of Amyloid β peptides associated with AD. Through the self-assembly of phosphotungstate, $K_8[P_2CoW_{17}O_{61}]$, and Aβ15-20 (Ac-QKLVFF-NH_2), Li et al. demonstrated the spontaneous formation of hybrid colloidal spheres in water, which

was predominantly driven by electrostatic interactions. Furthermore, the enhanced inhibition efficiency and specific targeted-Aβ ability have been considered important and useful in clinical treatment with reduced side effects of POM [54]. In addition, Lee et al. generated multivalent nanofibers through electrostatic interactions between polyoxometalates and short peptides. Because of the supramolecular nature of the ensemble, POMs thus enabled the enhancement of the antimicrobial efficacy and biological stability of short peptides in situ [55]. It is expected that the extraordinary properties of POMs could be used to develop hierarchical assemblies for the fields of biological chemistry and materials science.

In addition to their conventional hotspots as catalysts, antimicrobial and virus inhibitors, polyoxometalates are also attractive in many other applications. Eu-containing POM of $Na_9[EuW_{10}O_{36}]\cdot 32H_2O$ (EuW_{10}) shows the highest luminescent quantum yield and strongest fluorescence. Song et al. [56]. fabricated the well-ordered, ultra-thin films based on the hybrid assembly of $Na_9[EuW_{10}O_{36}]\cdot 32H_2O$ (denoted as EuW_{10}) and exfoliated MgAl layered double hydroxide (LDH) monolayers by utilizing the layer-by-layer (LBL) technique, as shown in

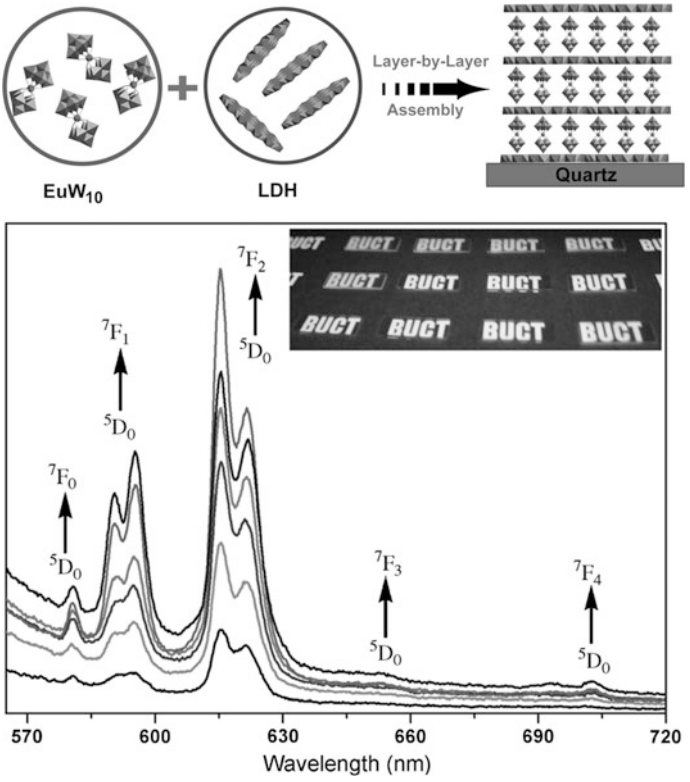

Fig. 14.5 **a** Schematic representation of the assembly process of the nanocomposite films of $(EuW_{10}/LDH)_n$. **b** Fluorescence spectra and photographs under UV irradiation at 254 nm with *n* increasing from 3 to 18. Reproduced from Ref. [56] by permission of John Wiley & Sons Ltd

Fig. 14.5. Anisotropic luminescence spectroscopy measurements show that the $(EuW_{10}/LDHs)_n$ ultra-thin films display well-defined red luminescence with an anisotropy value, r, of about 0.15. The cooperative and orientation effects between the LDH and polyanions play significant roles in the improved properties of the ultra-thin films. This work could benefit the design and fabrication of novel electro-optical devices based on the ultra-thin films of hybrid materials. The dream goal of energy research is to transpose incredibly efficient process and make an artificial device whereby the catalytic splitting of water is finalized to give a continuous production of oxygen and hydrogen.

This chapter is mainly devoted to a review of recent developments by our group in thin films formed by nanoengineered polyoxometalates and their various applications. Section 14.2 gives an overview of supramolecular architectures assembled from amphiphilic hybrid polyoxometalates, including the multilayer thin films, giant vesicles and onionlike structures. In Sect. 14.3, fabrication of honeycomb films of HSECs at air/water interface has been concluded, including the fabrication method, mechanism, morphology modulation and the promising applications of honeycomb films in detail.

14.2 Supramolecular Architectures Assembled from Amphiphilic Hybrid Polyoxometalates

One of the important aspects of POM clusters is their high solubility in a variety of solvents, which places POMs in a unique position as 'molecular' metal oxides. Mostly, POMs are ionized as giant anions (several nanometers) and countered by small cations, such as Na^+, NH_4^+, and H^+, in aqueous solutions, which is very different from the case for other metal-oxide materials. Once POMs are dissolved, the clusters interact electrostatically with cationic species, and this intrinsic driving force enables associations between POMs and cationic ions, molecules, complexes and polymers, as well as positively charged solid surfaces of materials. Consequently, POMs can be reliably modified through various techniques and methods to develop sophisticated materials and devices.

Hydrophilic POM macroions can interact with organic cations or cationic surfactants mainly through electrostatic interactions to construct inorganic-organic amphiphilic hybrids. One example is the surfactant encapsulated POM clusters (SECs). Kurth et al. created SECs by replacing the countercations of anionic molybdovanadato POMs by long alkyl chained cationic ammonium surfactants [57, 58]. A close packing of the alkyl chains was observed, and it was concluded that there is a compact shell around the POM. The surfactant shell improves the stability of the embedded POM as well as its solubility in nonpolar, aprotic organic solvents. Furthermore, it can change the surface chemical properties of POMs in order to realize the integration of multifunctional POMs into thin films and ordered three-dimensional aggregations.

14.2.1 Multilayer Films Containing POMs by Layer-by-Layer Technique on Planar Substrates

The origins of layer-by-layer assembly (LbL) can be traced back to the work of Iler in 1966, in which he fabricated multilayers by alternative deposition of positively and negatively charged colloid particles on planar surfaces [59]. It has been evolved as a powerful approach to produce different composite films on various types of substrates. Compared with other methods, the LBL technique has significant advantages in film stability and catalyst reusability. What is more, each nanometer-scaled POM molecule has a homogeneous diameter and surface charge when dissolved in a polar solvent. Our group fabricated the ultrathin films based on TiO_2 and tungstophosphate ($H_3PW_{12}O_{40}$, abbreviated as PW_{12}) by LbL self-assembly method on quartz, silicon, and ITO substrates and first applied them to photodegrade dye effluents [60]. Based on electrostatic interaction, $(TiO_2/PW_{12})_n$ multilayer films were fabricated and characterized on quartz slides, silicon wafers, and microscopic glass slides. These solid substrates were treated according to the literature [61]. The hydrophilic substrates were first immersed in poly(allylamine hydrochloride) (PAH) aqueous solution for 15 min, then rinsed by diluted $HClO_4$ solution at pH = 2.5 and dried by N_2. Subsequently, poly(styrenesulfonate) (PSS) was assembled in the same way as PAH. The procedure described above was repeated once to gain a surface with uniform charge. Then, the substrates with four precursor layers were alternately dipped in positively charged TiO_2 colloid (16 g L^{-1}, pH $\sim$ 2.0) for 15 min and 3 mmol L^{-1} negative charged PW_{12} solution for another 15 min until the desired number of bilayers was obtained. Rinsing and drying were conducted after each deposition cycle. The multilayer films with the desired number were described as $(TiO_2/PW_{12})_n$, where n was the number of bilayers. The $(TiO_2/PW_{12})_n$ composite films (with n = 2, 4, 6, 8, 10) are assembled on $(PAH/PSS)_2$ precursor film-coated quartz slides. The self-assembly process of multilayer films can be monitored by UV-vis spectroscopy, as shown in Fig. 14.6a. The $(PAH/PSS)_2$ precursor films show no absorbance in

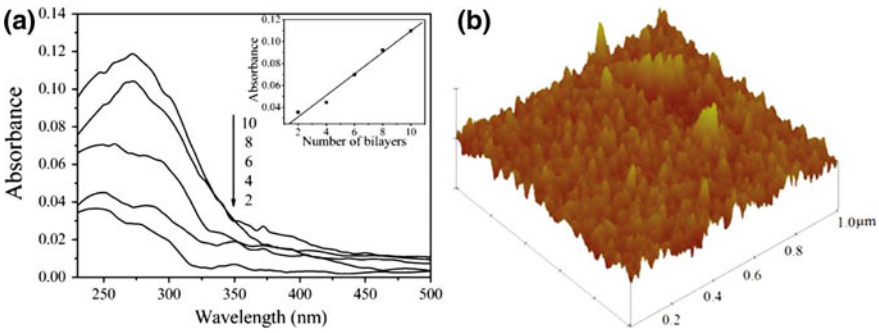

Fig. 14.6 **a** UV-vis spectra of the $(TiO_2/PW_{12})_n$ composite films assembled on quartz slides. Inset shows the relationship of absorbance at 253 nm versus the number of bilayers of $(TiO_2/PW_{12})_n$ films. **b** $(TiO_2/PW_{12})_4$ multilayer film assembled on silicon slides. Reprinted with the permission from Ref. [60]. Copyright 2011 American Chemical Society

230–500 nm UV-vis region. The maximum absorbance of composite films is 253 nm, which is attributed to charge transfer from O to W atom in the Keggin unit, increasing with TiO_2 and PW_{12} deposition. The inset shows the absorbance at 253 nm as a function of bilayer number and an approximately linear relationship is observed. The detailed information about the surface morphology and homogeneity of multilayer films are investigated by AFM (Fig. 14.6b).

In past decades, due to the low cost, innoxiousness, chemical inertness, and high photocatalytic performance, TiO_2 has been extensively used as photocatalysts for the degradation of organic dyes [62]. However, the photocatalytic efficiency of TiO_2 is remarkably decreased owing to the fast recombination of photogenerated electron hole pairs. POMs, considered efficient electron acceptors, can successively transfer the photogenerated electrons from the TiO_2 conduction band to the empty d orbital of theirs, which can improve the photocatalytic efficiency owing to the synergistic effect of POMs and TiO_2. In order to evaluate the photocatalytic efficiency of the composite films, methyl orange (MO), was used as a probe for the photocatalytic degradation. The maximum absorption peak of MO shifts from 463 nm under nearly neutral condition to 487 nm at pH 4.0 and to 507 nm at pH 2.0, which is due to the delocalization of lone pair electrons on the azo group in two different structure of MO. We carried out the photocatalytic tests at pH 2.0. Figure 14.7a shows the UV-vis absorption spectra changes of aqueous MO (10 mg mL^{-1}) solution in the presence of $(TiO_2/PW_{12})_n$ composite films. The intensity of MO absorption peaks gradually decreases as irradiation time increases, which suggests that MO is almost completely decomposed. The kinetics of MO photodecomposition by composite films with different number of bilayers was investigated. The plots of $\ln c_0/c$ (where c_0 stands for the initial concentration and c is the residual concentration at time t) versus time for MO photodegradation are shown in Fig. 14.7b, which indicates that photodecomposition of diluted MO solutions agrees well with apparent first-order kinetics.

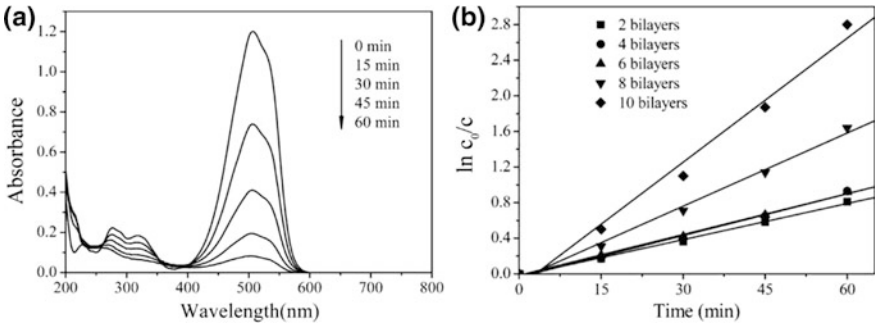

Fig. 14.7 **a** UV-vis absorption spectra changes of MO (10 mg L^{-1}, pH = 2.0) solution in the presence of $(TiO_2/PW_{12})_{10}$ composite films. **b** Reaction kinetic study of photodegradation of MO (the initial concentration: 10 mg L^{-1}, pH = 2.0) by $(TiO_2/PW_{12})_n$ films. Reprinted with the permission from Ref. [60]. Copyright 2011 American Chemical Society

Coincidentally, we demonstrated polyoxometalates which have different compositions, shapes, and sizes can interact with TiO_2 to self-assemble into multilayer film on silicon wafers and glass slides for photocatalytic degradation of methyl orange (MO). We choose nano-scaled POMs with different shapes, sizes, and compositions, including $H_4SiW_{12}O_{40}$ (SiW_{12}) [62, 63] and $Na_4W_{10}O_{32}$ ($W_{10}O_{32}$) [64], to be the typical examples. The main role of surfactants in dyeing processes is to increase the solubility of dyes in water and improve the dye-uptake and dye fastness, to reduce the dyeing temperature. In fact, actual dye wastewaters contain not only dyes, but also other auxiliaries such as salts and surfactants. Therefore, to make sure the effect of surfactants and salts in the MO degradation process is a burning question. In our study, photocatalytic processes were performed in the presence of two inorganic salts and two different surfactants, NaCl, Na_2SO_4, sodium dodecylsulfate (SDS, cmc = 8.6 mmol L^{-1}), and polyoxyethylene dodecyl ether ($C_{12}E_{23}$, cmc = 0.043 mmol L^{-1}). Figures 14.8a, b turn out that the presence of inorganic salts, especially Na_2SO_4, exhibits an obvious inhibition effect on the MO degradation. The removal efficiency of dye is deceased when the concentration of inorganic salts is increased. The difference between two inorganic salts may be mostly due to the aggregation or association of ionic dye in water. As shown in Figs. 14.8c, d, the surfactants with different types exhibit two completely different results. It can be observed that the nonionic surfactant shows the excellent

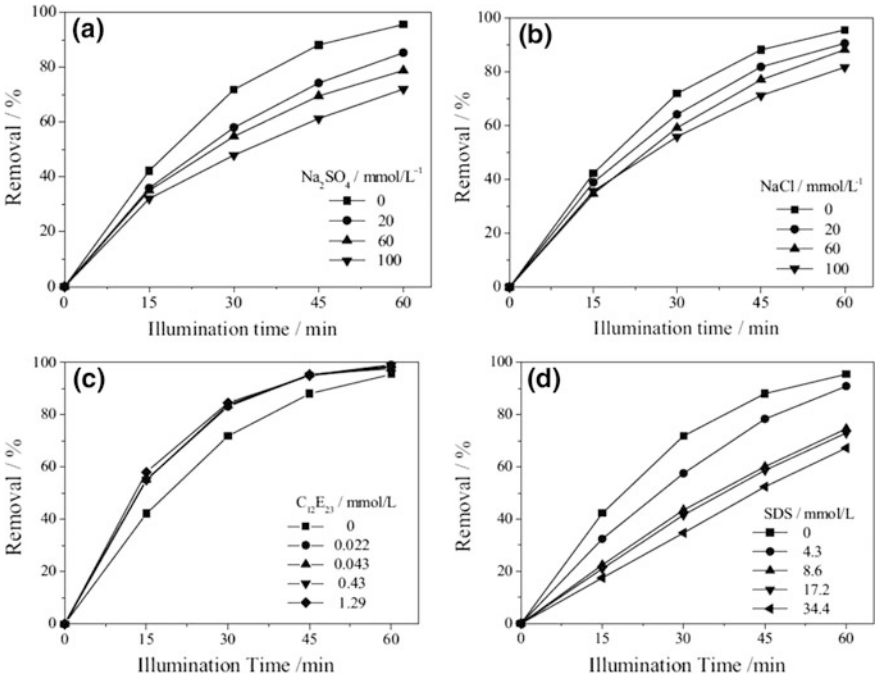

Fig. 14.8 Removal efficiency of MO at different concentration of inorganic salts: **a** Na_2SO_4 and **b** NaCl and **c** $C_{12}E_{23}$ and **d** SDS. Reprinted from Ref. [63], Copyright 2014, with permission from Elsevier

acceleration effect on the photocatalytic degradation of MO, while for the anionic surfactant SDS, a markedly suppressing effect is observed. For $C_{12}E_{23}$, oxygen in the EO groups of $C_{12}E_{23}$ has extra lone pairs of electrons,while W atom of SiW_{12} polyanions has empty d orbitals. Hence, SiW_{12} polyanion and nonionic surfactant $C_{12}E_{23}$ can form a weak complex through electrostatic interaction, which is responsible for the enhancement of MO removal efficiency. Contrary to $C_{12}E_{23}$, in premicellar or micellar regions formed by anionic surfactant SDS, ionic pairs formed due to the weak interaction between dye and SDS first adhere to the micelles surfaces, and then incorporate into the micelles, in which MO may become inert to react with TiO_2/SiW_{12} composite films. This work will provide valuable information for the researchers who engage in treatment of textile effluents.

14.2.2 Self-patterning Porous Films Composed of POMs-Based Giant Vesicles

Cationic surfactants with long enough alkyl chains can interact with POMs stoichiometrically through electrostatic interaction, which can improve the stability of POMs in nonpolar solvent and change the interface property of POMs. Therefore, cationic surfactants encapsulated POMs macroanions can transfer from water to organic solution for forming POMs/surfactants complexes. These organic-inorganic nanoscale hybrids can change the surface property of POMs to be hydrophobic in behavior. These complexes still retain amphiphilic property to dissolve in organic solvents and self-assemble to form various ordered aggregates such as thin hybrid films [63], vesicles [66], liquid crystals [67, 68], gels with the structures of fibers [69], and so on. Many groups have reported single- or multi-layer films fabricated by POMs. However, to the best of our knowledge, very few self-assembled three dimensional structures based on POMs and organic components were used to fabricate films as building blocks. Conceptually, we reported a new fabrication of the complexes by a Keplerate-type polyoxomolybdate, $\{Mo_{72}Fe_{30}\}$, and a double-chain cationic surfactant DODMABr to produce the giant inverse vesicles in organic solvent [70]. The 2.5-nm-diameter, "Keplerate" molecule $\{Mo_{72}Fe_{30}\}$ exists as almost neutral molecules in crystals, but in solution they behave like a weak acid: the water ligands attached to the Fe^{III} centers tend to partially deprotonate, thus making $\{Mo_{72}Fe_{30}\}$ clusters slightly negatively charged (carrying several localized charges). The degree of deprotonation depends on the solution pH, from almost 0 at pH 3.0–22 at pH 4.9. When the $\{Mo_{72}Fe_{30}\}$ aqueous solution mixed with enough amount of cation surfactant dioctadecyldimethylammonium chloride (DODMABr), $\{Mo_{72}Fe_{30}\}$ can be transfer into the organic phase (chloroform phase) by forming the hydrophobic DODMABr-$\{Mo_{72}Fe_{30}\}$ complexes through electrostatic interactions between the $\{Mo_{72}Fe_{30}\}$ anions and the $DODMA^+$ cations. The yellow color of the aqueous phase (from $\{Mo_{72}Fe_{30}\}$) continuously vanishes, while the color of the $CHCl_3$ phase turns gradually yellow.

In order to determine the composition of DODMABr-{$Mo_{72}Fe_{30}$} complexes, the negative charge number of {$Mo_{72}Fe_{30}$} polyanions can calculate by an exponential equation:

$$N_{\{Mo72Fe30\}} = M_{\{Mo72Fe30\}} 10^{-pH\{Mo72Fe30\}} / c_{\{Mo72Fe30\}}$$

where $N_{\{Mo72Fe30\}}$ is the negative charge number of {$Mo_{72}Fe_{30}$} polyanions; $M_{\{Mo72Fe30\}}$ is the molecular weight of {$Mo_{72}Fe_{30}$}; $pH_{\{Mo72Fe30\}}$ is the pH value of {$Mo_{72}Fe_{30}$} aqueous solution and $c_{\{Mo72Fe30\}}$ is the concentration of {$Mo_{72}Fe_{30}$} aqueous solution.

In this study, {$Mo_{72}Fe_{30}$} aqueous solution has a certain concentration is 8 mg mL^{-1} {$Mo_{72}Fe_{30}$} and the pH value is 2.91. So the composition of {$Mo_{72}Fe_{30}$}/DODMABr complexes could be calculated to be {$Mo_{72}Fe_{30}$} $(DODMA)_3$. In the $CHCl_3$-CH_3OH (3:1)mixed solution, {$Mo_{72}Fe_{30}$} $(DODMA)_3$ complex can form densely packed multilamellar inverse vesicles due to the larger inorganic polar head groups comparing to conventional surfactants.

Densely packed multi-lamellar inverse vesicles in organic solution via self-assembly formed by the {$Mo_{72}Fe_{30}$}$(DODMA)_3$ complexes were demonstrated by the SEM and TEM observations (Fig. 2.4). Differing from normal vesicles, reverse vesicles are those with hydrophilic groups inwards and hydrophobic countparts outwards arranged in non-aqueous solutions. Figures 14.9a, b show two different types of spherical vesicles and spherical vesicles with collapse parts. TEM images indicated the enlarged image of part of a multilayer vesicle, which were the hollow sphere composed of small particles with the average 2.47 ± 0.07 nm in diameter, which exactly corresponds to the size of a {$Mo_{72}Fe_{30}$}. Furthermore, the bilayer thickness of the {$Mo_{72}Fe_{30}$}$(DODMA)_3$ vesicles can be calculated to be about 7.3 nm according to the extended chain length of double chain cationic DODMABr (2.4 nm) [71] and the diameter of {$Mo_{72}Fe_{30}$} (2.5 nm). The average wall thickness of the vesicle is about (50.6 ± 13.0) nm from Fig. 14.9, thus the vesicles of the {$Mo_{72}Fe_{30}$}$(DODMA)_3$ complexes are about (7 ± 2) bilayers.

The giant vesicles can self-assemble to form porous films on solid surfaces via the breath figure method. When the {$Mo_{72}Fe_{30}$}$(DODMA)_3$ complexes were prepared by 0.3 mL {$Mo_{72}Fe_{30}$} aqueous solution (8 mg mL^{-1}) mixed with DODMABr organic solution, the relatively excess hydrophobic DODMABr molecules exist on the single crystal silicon slides, water permeation on substrate surfaces was hampered and the humid nitrogen stream could not drive the {$Mo_{72}Fe_{30}$}$(DODMA)_3$ complexes to form porous films (Fig. 14.10a). Increasing amount of {$Mo_{72}Fe_{30}$} to 0.45 mL in DODMABr organic solution, as shown in Fig. 14.10b, the porous structures became clearer and the porous films can easily be obtained, but the pore size is polydispersed from 200 nm to more than 2.0 μm. With a further increase amount of {$Mo_{72}Fe_{30}$} to 0.6 mL, highly ordered porous films with large size holes of 7–10 μm (Fig. 14.10d) surrounding pores with uniform sizes of 1.0 μm (Fig. 14.10e) can be successfully obtained by large areas. In order to observe the interior structure of the porous films more distinctly,

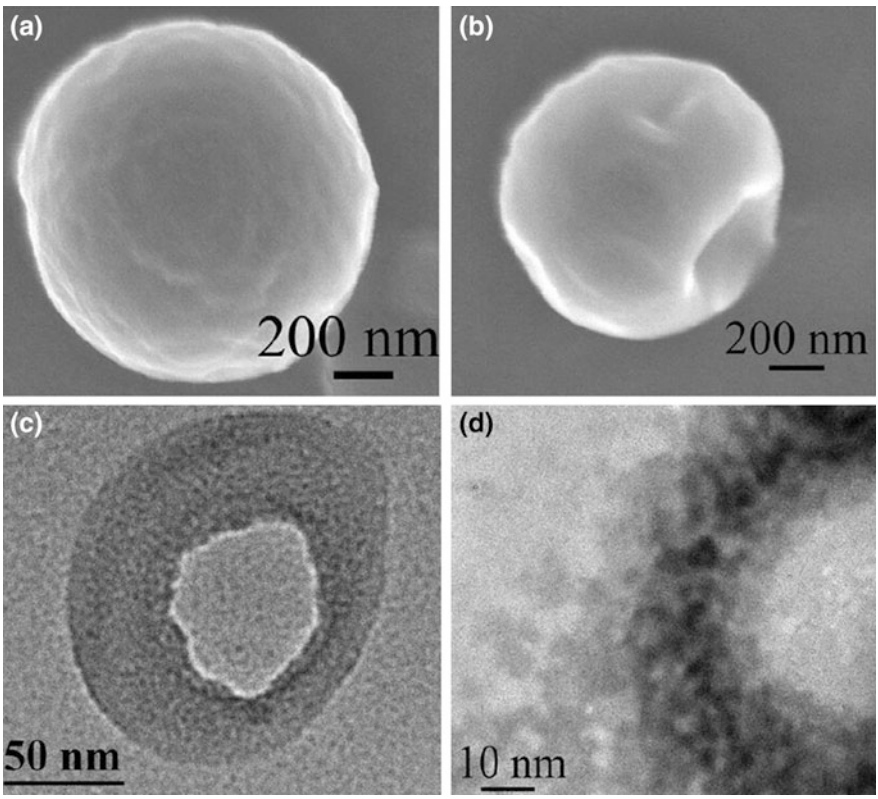

Fig. 14.9 **a**, **b** SEM enlarged images. **c**, **d** TEM enlarged images of giant inverse vesicles of $\{Mo_{72}Fe_{30}\}(DODMA)_3$ complexes in organic phase. Reprinted from Ref. [70], Copyright 2016, with permission from Elsevier

a cross-sectional view of the porous films was shown in Fig. 14.10f. The interior of porous films are filled with giant vesicles in a regular arrangement, indicating the giant vesicles acted as building blocks of the porous films. The structure of giant vesicles is reserved completely during the process of organic solvent evaporation because of higher structural strength. In order to further analyze the porous film structures formed by the vesicles of the $\{Mo_{72}Fe_{30}\}(DODMA)_3$ complexes, the XPS analysis of the porous film surface was characterized. The high resolution XPS spectra of C1 s were devided into two peaks centered at 284.7 and 286.4 eV, which are attributed to C–H/C–C and C–N, respectively. The high resolution XPS spectra of N1 s were deconvoluted into three peaks centered at 398.7, 399.9 and 403 eV (Fig. 14.11b). The major peak at 399.9 eV was attributed to C–N. The peak at 402–403 eV was selectively attributed to N^+OH^- inter- and intra-molecular hydrogen bond, and the weak peak at 403 eV resulted from the interaction between small amount of $\{Mo_{72}Fe_{30}\}$ anions and $DODMA^+$. Meanwhile, N1 s binding energy of the C–N bond is decreased because of the interaction of $\{Mo_{72}Fe_{30}\}$ macroanions

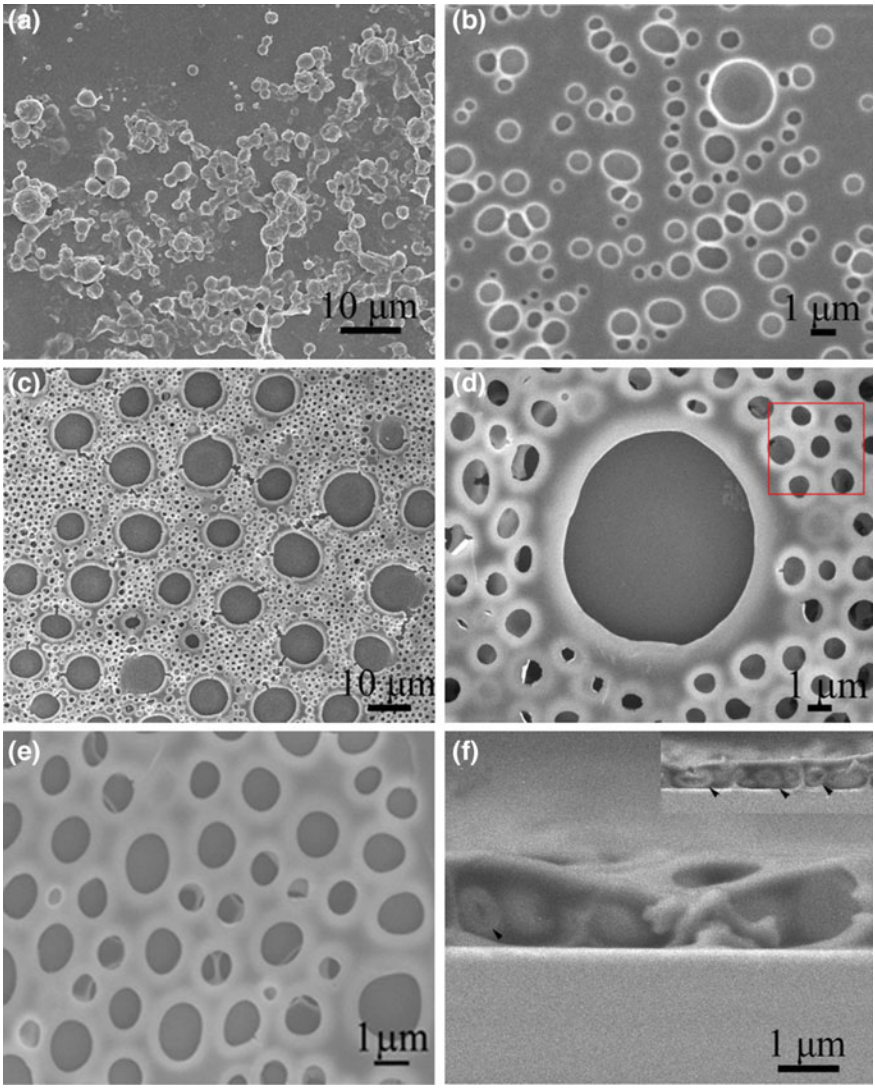

Fig. 14.10 FE-SEM images of porous films of vesicles formed by $\{Mo_{72}Fe_{30}\}(DODMA)_3$. The organic solution of $\{Mo_{72}Fe_{30}\}(DODMA)_3$ vesicles were prepared by different volumes of 8 mg mL^{-1} $\{Mo_{72}Fe_{30}\}$ aqueous solution equilibrated with 4 mL 1 mg mL^{-1} DODMABr in $CHCl_3$–CH_3OH (3:1) solution for 2 weeks. $V_{\{Mo72Fe30\}}$ = 0.30 mL (**a**), 0.45 mL (**b**), 0.6 mL (**c**, **d**). An enlarged image of the wall of the porous films (**e**) and a cross-sectional survey of the chosen area arbitrarily marked with red rectangle in Fig. 14.10d, one can see the vesicles with collapsed parts (*arrows marked*, **f**). Reprinted from Ref. [70], Copyright 2016, with permission from Elsevier

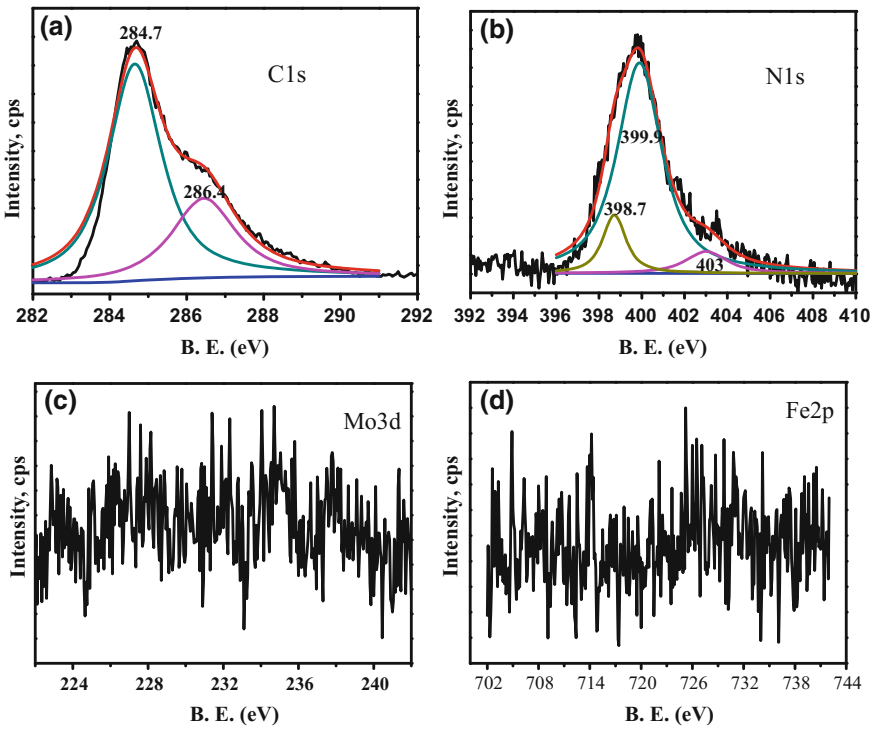

Fig. 14.11 High resolution XPS spectra of C1s (**a**), N1s (**b**), Mo3d (**c**) and Fe2p (**d**) of porous films of vesicles formed by $\{Mo_{72}Fe_{30}\}(DODMA)_3$. The organic solution of the $\{Mo_{72}Fe_{30}\}(DODMA)_3$ vesicles were prepared by 0.6 mL 8 mg mL^{-1} $\{Mo_{72}Fe_{30}\}$ aqueous solution equilibrated with 4 mL 1 mg mL^{-1} DODMABr in $CHCl_3$–CH_3OH (3:1) solution. Reprinted from Ref. [70], Copyright 2016, with permission from Elsevier

and $DODMA^+$, result in a weak peak appeared at 398.7 eV. However, as shown in Fig. 14.11c and d, no obvious peaks appeared in the high resolution XPS spectra of Mo3d and Fe2p, indicating that the surface of the porous films were mainly formed by excess DODMABr, and probably had few $\{Mo_{72}Fe_{30}\}(DODMA)_3$ complexes.

In order to investigate whether the honeycomb films can form by changing the composition of $\{Mo_{72}Fe_{30}\}$/DODMABr complexes. Another $\{Mo_{72}Fe_{30}\}$/(DODMA) complexes in organic phase formed by adjusting the concentration of $\{Mo_{72}Fe_{30}\}$ aqueous solution to 1 mg mL^{-1}. In this case, seven H^+ ions can be released from one $\{Mo_{72}Fe_{30}\}$ molecule in aqueous solution, in which the $\{Mo_{72}Fe_{30}\}(DODMA)_7$ complexes were obtained. The vesicles formed by $\{Mo_{72}Fe_{30}\}(DODMA)_7$ complexes are much smaller than those formed by $\{Mo_{72}Fe_{30}\}(DODMA)_3$ complexes. When the same volume of aqueous solution was mixed with the $CHCl_3$–CH_3OH (3:1) organic solution, almost all CH_3OH in organic phase was transferred into aqueous solution, $\{Mo_{72}Fe_{30}\}(DODMA)_7$ vesicles retained in $CHCl_3$ phase. Giant vesicles cannot be formed because of weak

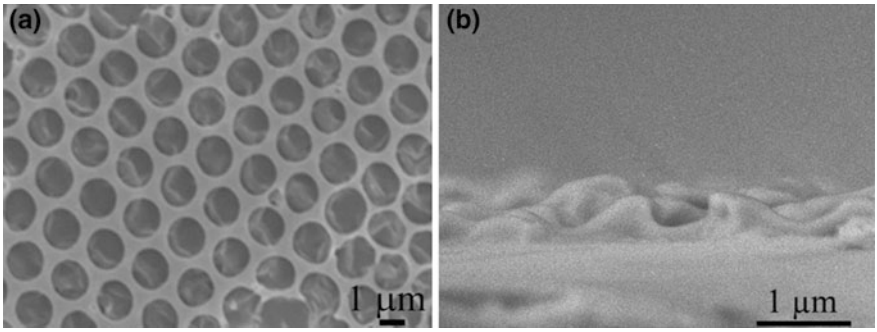

Fig. 14.12 FE-SEM images of highly ordered honeycomb films of the $\{Mo_{72}Fe_{30}\}(DODMA)_7$ complexes formed by 4 mL 1 mg mL^{-1} DODMABr in $CHCl_3$-CH_3OH (3:1) solvent equilibrated with 4 mL 1 mg mL^{-1} $\{Mo_{72}Fe_{30}\}$. Surface morphology (**a**) and a cross-sectional survey (**b**). Reprinted from Ref. [70], Copyright 2016, with permission from Elsevier

polarity of organic solvent. The highly ordered honeycomb films were prepared on single crystal silicon slides by dropping the $CHCl_3$ solution of $\{Mo_{72}Fe_{30}\}(DODMA)_7$ complexes, as shown in Fig. 14.12a. In this case, we cannot see the vesicles composed of $\{Mo_{72}Fe_{30}\}(DODMA)_7$ complexes situated interior the porous films. It must be because the vesicles of the $\{Mo_{72}Fe_{30}\}(DODMA)_7$ complexes were too small to be survived the drying process in preparation of honeycomb films via breath figure method (Fig. 14.12b). This phenomenon demonstrates that the concentrations of POMs and surfactants play an important role in the preparation of highly ordered honeycomb films.

14.2.3 Robust Onionlike Structures Formed by a Fullerene C_{60}-POM Hybrid

Polyoxometalates (POMs) have remarkable properties and a great deal of potential to meet contemporary societal demands regarding health, environment, energy and information technologies. However, implementation of POMs in various functional architectures, devices or materials requires a processing step. Most developments have considered the modification of POMs through non-covalent or covalent interaction. We have discussed the interaction of POMs and surfactants through non-covalent in Sects. 14.2 and 14.3. In this section, we will investigate the covalent modification. The covalently modified amphiphilic hybrid POMs are attractive. Some POM clusters possess multiple sites available for functionalization, which can be done by linking one or more hydrophobic organic functional groups to one POM. In addition, the amphiphilic nature of these hybrids extends the functionality of POM clusters in organic media, which used as multifunctional oxidation or acidification catalysts with good selective recognition of substrates.

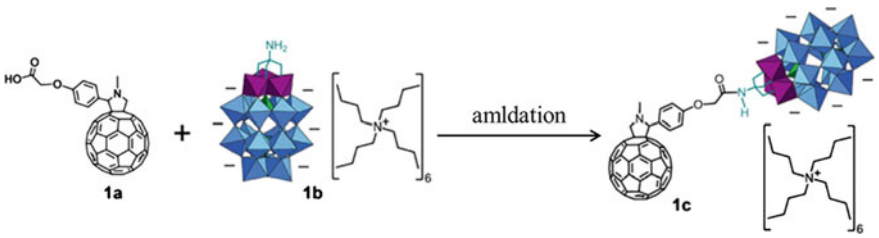

Fig. 14.13 Synthetic route to fullerene C_{60}-Dawson POM hybrid compound **1**. Reproduced from Ref. [72] by permission of the Royal Society of Chemistry

In view of the outstanding optical, electrochemical and photodynamic activities of C_{60} and well-known magnetic and catalytic properties of POMs, the idea of covalently linking them to create a new class of amphiphiles becomes quite attractive. However, C_{60}-POM hybrids as structural models are rarely reported. Recently our group reported the synthesis and aggregation behavior of a fullerene C_{60}-Dawson POM hybrid (**1**) for the first time [72]. Our strategy (Fig. 14.13) to create **1** includes amide coupling between a monosubstituted C_{60} carboxylic acid (**1a**) and a tris-modified, Dawson trivanadium substituted heteropolytungstate (**1b**) in a THF/CH_3CN mixture solvent. C_{60} exhibits poor solubility in polar solvents including DMSO, DMF and CH_3CN while Dawson POMs are not. After covalent attachment, **1** shows quite a similar solubility to the POM moiety, may due to the larger size of Dawson POM compared to C_{60}. The compound **1** possesses unique amphiphile molecular structure, resulting in dissolving in these POM-friendly solvents with the C_{60} unit as the solvophobic part. We first checked the aggregation behavior of **1** in DMSO and the typical results are summarized in Fig. 14.14. Observations of two typical samples showed the formation of vesicles with diameters of 30–110 nm (image Fig. 14.14a, b). From the high resolution TEM (HRTEM, image c,) we can see the thickness of an individual layer is $\sim$3.5 nm (between the arrow heads) and a distance of 5.0 nm between two adjacent layers (averaged from four repeating units indicated between the two arrows). In scanning electron microscopy (SEM) observations (image d), contrast variations have also been noticed at the edges of the onionlike aggregates, which further confirms a core-shell structure.

Multiple intermolecular forces including solvent-phobic interaction, van der Waals attraction and p–p stacking among C_{60} spheres as well as electrostatic interaction and the like-charge attraction among POM units driven the formation of the onionlike structures demonstrated here. We presumed a structural model of molecular bilayers with the POM units staying outside and C_{60} moieties hiding inside, which can be proofed from, as shown in Fig. 14.15, ^{13}C NMR where signals of the carbon atoms from C_{60} appear as a bulge between 140 and 150 ppm, which is in sharp contrast to those of C_{60} monoadducts in a good solvent, which exist as a variety of sharp peaks in the same region. It can be speculated that a structural model of molecular bilayers can be envisaged with the POM units staying outside

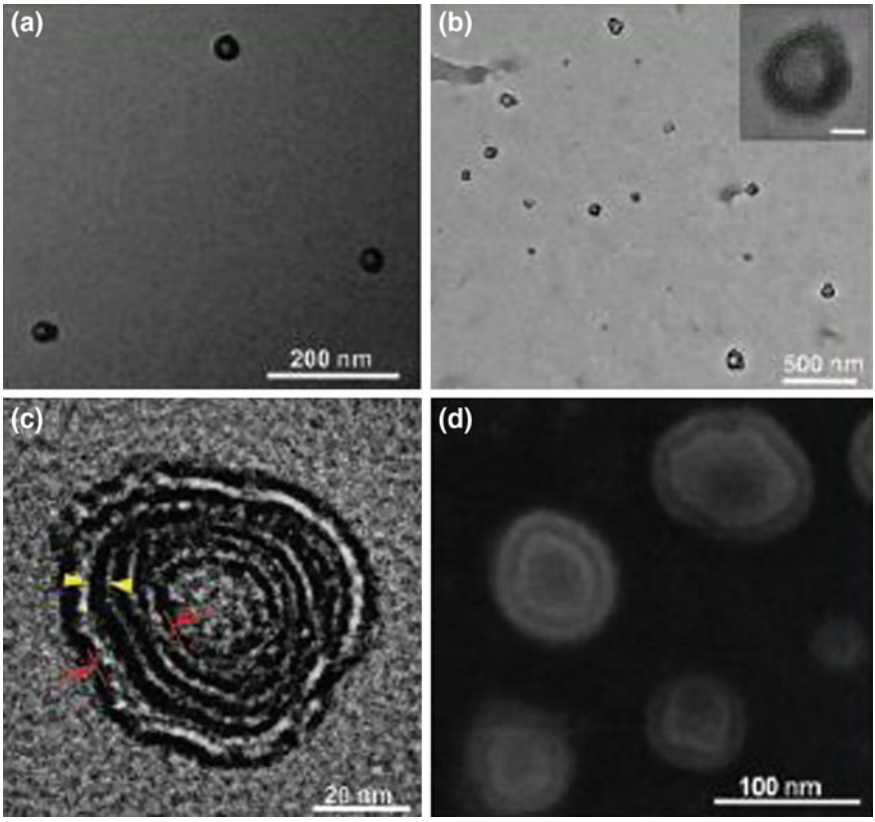

Fig. 14.14 Self-assembly of compound **1** in DMSO. TEM (**a**, **b**), HRTEM (**c**) and SEM (**d**) images. The concentration of **1** is 5.0 (**a**, **d**) and 20.0 (**b**, **c**) mg mL^{-1}, respectively. The scale bar for the magnified image inside image **b** is 20 nm. Reproduced from Ref. [72] by permission of the Royal Society of Chemistry

and C_{60} moieties hiding inside. Therefore, the C_{60} spheres are internally encapsulated in a quasi-solid state with obvious inter-sphere interactions upon aggregate formation. In addition, the aggregate formation also leads to peak broadening and baseline roughening in ^1H NMR (Fig. 14.15), which is consistent with similar phenomenon observed for alkyl chains embedded in molecular aggregates in water, such as vesicles. When solvents replaced by other solvents with similar polarities, such as CH_3CN and DMF, onionlike structures with similar sizes and number of layers also can be obtained. Interestingly, the onionlike structures exhibit high resistance towards the addition of water. The solutions remain stable up to the addition of 99% (v/v) water for the two series of samples with 5.0 and 0.6 mg mL^{-1} **1** in DMSO. The relatively strong interactions among the C_{60} units in water as well as the decreased water solubility of the POM moieties are contributed to the robustness of the onionlike structures towards the addition of water.

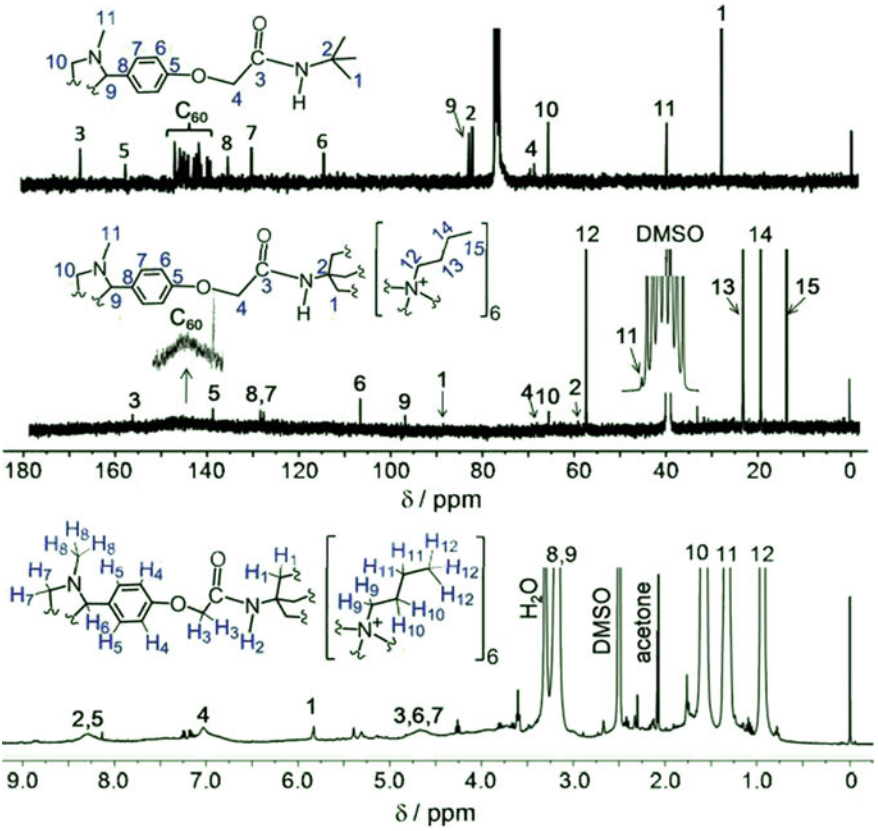

Fig. 14.15 *Top* ^{13}C NMR of the monosubstituted C_{60} carboxylic ester (1a″, in $CDCl_3$) and **1** (in d6-DMSO). Bottom: ^{1}H NMR of **1** (in d6-DMSO). The C_{60} unit and POM moiety has been omitted in the molecular structures for better clarity. Reproduced from Ref. [72] by permission of the Royal Society of Chemistry

The onionlike structures formed by compound **1** have rich physicochemical properties originating from both C_{60} and POM moieties, which makes them thoroughly different from their counterparts formed by surfactant mixtures [73, 74]. The magnetic properties of **1** both in the solid state and bulk solutions were investigated by electron spin resonance (ESR) measurements, as shown in Figs. 14.16a, b. Compared to that in the solid state as evidenced by the well-defined anisotropic eight-line splittings of the $^{23}V(IV)$ nuclei derived from the POM unit (Fig. 14.16b), an un-splitting single line was noticed within the whole investigated temperature range, which can be ascribed to the faster spin-lattice interaction in bulk solution due to the formation of aggregates. Furthermore, the electrochemical properties of **1** along with the two precursor molecules 1a and 1b have been investigated by cyclic voltammetry (Fig. 14.16c). C_{60} and their derivatives are well-known for their capability of the production of singlet oxygen ($^{1}O_2$) under light. Figure 14.16d

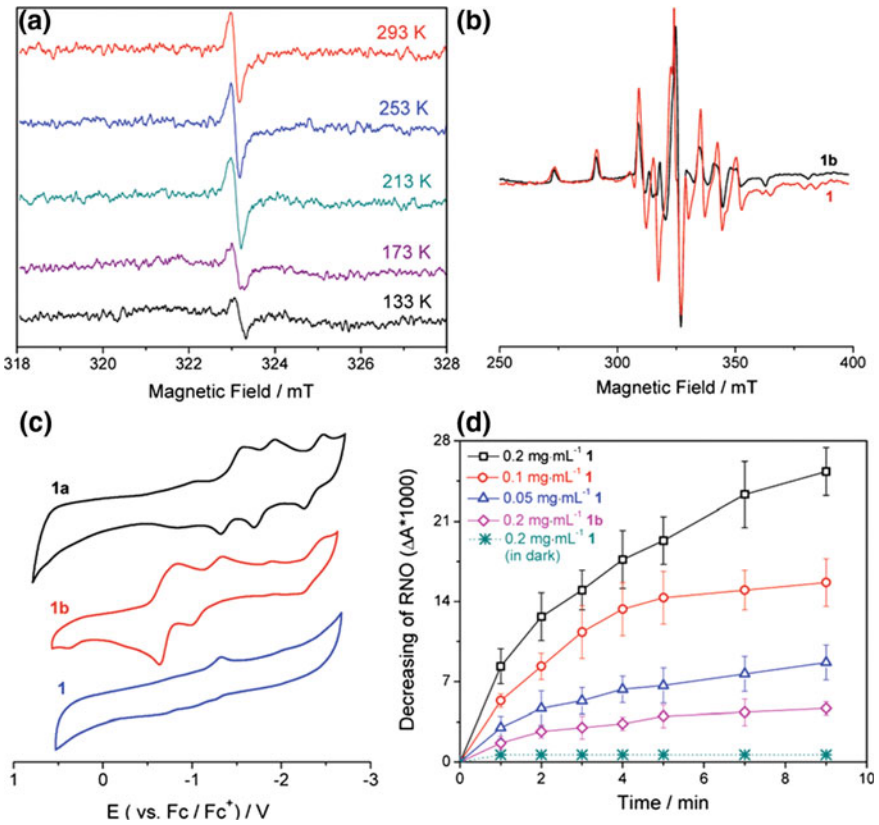

Fig. 14.16 **a** Temperature-dependent ESR spectra of 5.0 mg mL^{-1} **1** in CH_3CN. **b** ESR spectra of 1b and 1 in the solid state at room temperature. **c** Cyclic voltammetry of 1a (in dichlorobenzene), 1b (in DMF) and 1 (in DMF) with 0.1 mol L^{-1} tertbutylammonium hexafluorophosphate as the supporting electrolyte. **d** Generation of $^1O_2$ for **1** in aqueous solutions containing 1% (by volume) DMSO under 532 nm green light with a power density of 0.1 W cm^{-2}. For comparison, the activity in the dark is also given. Reproduced from Ref. [72] by permission of the Royal Society of Chemistry

shows the capability of $^1O_2$ production observed in the onionlike structures can be unambiguously attributed to the presence of the C_{60} unit. Moreover, a dose-dependent manner has been revealed under the irradiation of green light. The photodynamic properties of the onionlike structures indicate that the C60 moieties well preserve the capability of $^1O_2$ production even trapped in the molecular bilayers. This is exciting, considering the great potential of the biological activities exhibited by onionlike structures formed by compound **1** in biomedicine.

14.3 Self-assembled Honeycomb Films of Hydrophobic Surfactant-Encapsulated Clusters (HSECs) at Air/Water Interface

Nature provides inexhaustible inspiration to mankind, which continues to encourage us to develop new methods and approaches to the construction of artificial advanced materials. Bees, the artificers in nature, always build their hives in a hexagonal arrangement to minimize work and enhance the stability of the hive. In 1994, Francois et al. [75]. developed the polymeric porous honeycomb film with hexagonally arranged pores 0.2–10 μm in diameter, walls 0.1–0.2 μm thick, and 10–30 μm high prepared by exposing a drop of polystyrene-b-polyparaphenylene solution in carbon disulfide (CS_2) to a flow of moist air. As shown in Fig. 14.17, the micrometer-sized pores exhibited a highly regular hexagonal arrangement, which are similar to the natural hive. From then on, many researchers made efforts to fabricate the honeycomb porous film by various materials and methods. Colloidal sphere templates [76, 77], emulsion templates [78], and other "lithograph" [79] have been used to construct ordered porous arrays with controlled pores in a long range by replicating periodic structures from inorganic oxides, colloidal metal particles, and polymers. In 2005, Wu et al. found that the surfactant-encapsulated POMs can self-assemble into vesicles in chloroform solution and can be further transferred into three-dimensional microporous architectures under moist air [80], which created opportunities for combining inorganic chemistry and colloidal surface chemistry, allowing us to fabricate microsized patterns of inorganic functional units through stepwise self-assembly of preorganized building blocks.

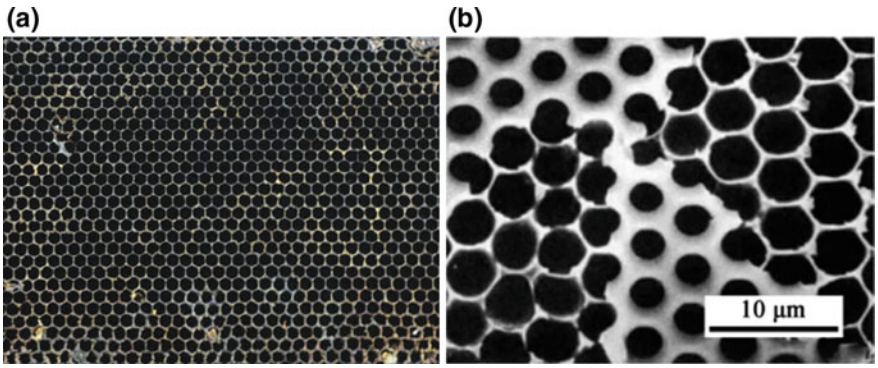

Fig. 14.17 **a** Photograph of natural hive built by worker-bees. **b** SEM image of PS-b-PPP honeycomb film. Reprinted by permission from Macmillan Publishers Ltd: Ref. [75], copyright 1993

14.3.1 Fabricating Honeycomb Films of HSECs at Air-Water Interface

Hydrophilic POMs of different sizes and shapes can interact with hydrophobic cationic surfactants, the resulting materials show amphiphilic properties with electrostatic interactions between the hydrophilic and hydrophobic components, called Surfactant-Encapsulated Clusters (SECs) or Surfactant-Encapsulated-POMs (SEPs), which can further self-assemble to give a variety of nanostructures on various surfaces/interfaces.

Our research group presented a unique system in 2007 [81]. We report the unprecedented self-assembly of hydrophobic double-chain cationic surfactant hybrid materials DODMACl-{$Mo_{72}Fe_{30}$} at the air/water interface without any extra airflow, which leads to the formation of highly ordered honeycomb films.

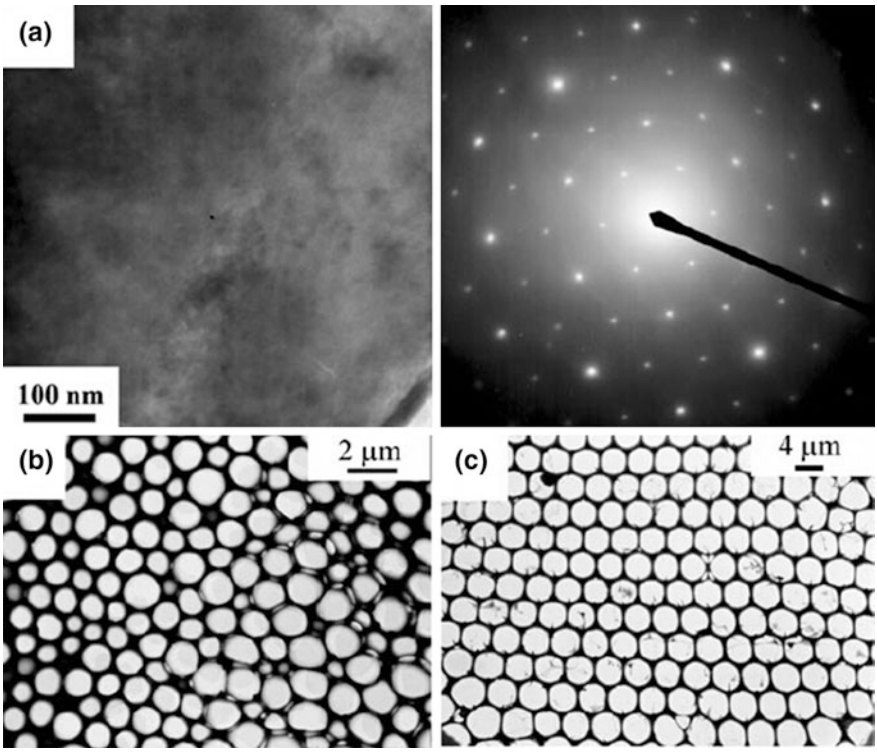

Fig. 14.18 **a** TEM images (*left column*) and the corresponding electron diffraction patterns (*right column*) of organized crystalline-structured monolayer films. TEM images of {$Mo_{72}Fe_{30}$}-DODMA complexes at **b** $c_{DODMACl}$ = 1.2 mg mL^{-1} and **c** $c_{DODMACl}$ = 2.0 mg mL^{-1} in $CHCl_3$. Reproduced from Ref. [80] by permission of John Wiley & Sons Ltd

In this study, we use the 2.5-nm-diameter, "Keplerate" molecule $\{Mo_{72}Fe_{30}\}$ as our model system, and they can interact with cation surfactant dioctadecyldimethylammonium chloride (DODMACl) to form the DODMACl -$\{Mo_{72}Fe_{30}\}$ complexes in organic solvent, which has discussed in Sect. 14.2.2 in detail. Then, an amount of $CHCl_3$-phase solution of DODMACl-$\{Mo_{72}Fe_{30}\}$ complexes was dropped onto a pure water surface, the honeycomb nanostructures of $\{Mo_{72}Fe_{30}\}$-DODMA complexes formed after evaporating $CHCl_3$, as shown in Fig. 14.18.

We demonstrated that the regularity of honeycomb architectures heavily depends on the surfactant concentration, given the fixed $\{Mo_{72}Fe_{30}\}$ concentration in aqueous solution. When the DODMACl concentration is lower than 1.2 mg mL^{-1} in $CHCl_3$, $\{Mo_{72}Fe_{30}\}$-DODMA complexes formed organized crystalline structures at the air/water interface by the packing of the complexes. When the concentration of DODMACl reaches 1.2 mg mL^{-1} in $CHCl_3$ ($c_{DODMACl}$ = 2.02 mmolL^{-1}), unique self-assembly of $\{Mo_{72}Fe_{30}\}$-DODMA complexes into honeycomb nanostructures was observed, as shown in Fig. 14.18b. The thickness of the wall between pores is in general smaller than 0.5 μm and the pore sizes are not

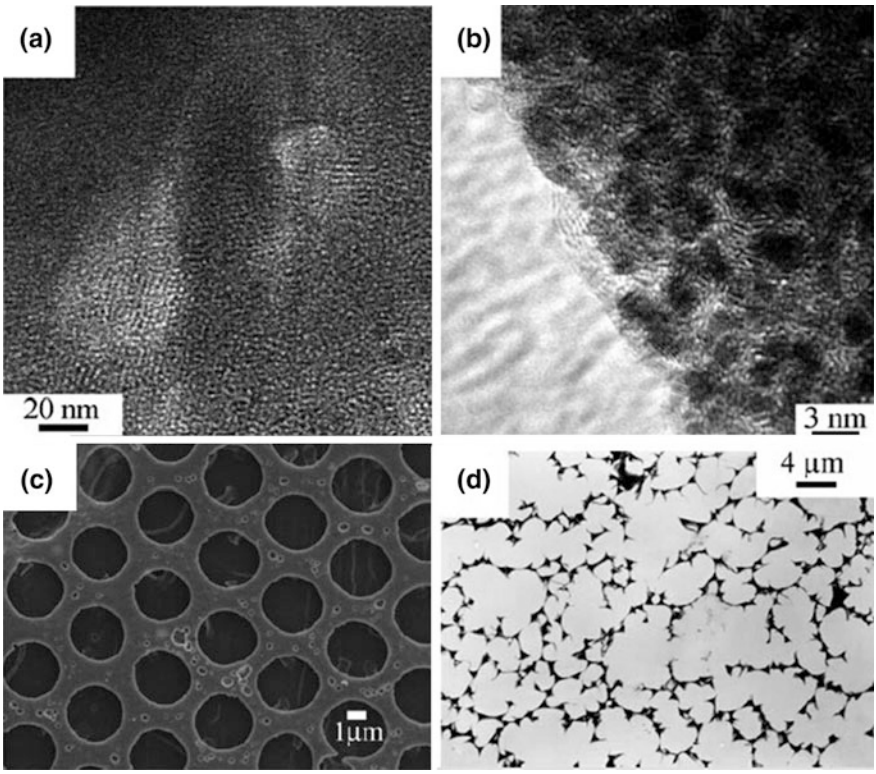

Fig. 14.19 **a**, **b** HRTEM images of the highly ordered honeycombs, which reveal the ordered texture with $\{Mo_{72}Fe_{30}\}$ at $c_{DODMACl}$ = 2.0 mg mL^{-1} in $CHCl_3$. **c** SEM image of highly ordered honeycomb architectures of $\{Mo_{72}Fe_{30}\}$-DODMA complexes. **d** TEM image of $\{Mo_{72}Fe_{30}\}$-DODMA complexes at $c_{DODMACl}$ = 4.0 mg mL^{-1} in $CHCl_3$. Reproduced from Ref. [80] by permission of John Wiley & Sons Ltd

homogeneous, ranging from 0.5 to 1.5 μm. At $c_{DODMACl}$ = 2.0 mmolL^{-1}, the nanostructure formed by {$Mo_{72}Fe_{30}$}-DODMA complexes (Fig. 14.18c) becomes more orderly, with honeycomb holes of uniform pore size (3.5 μm). The average thickness of the walls between the pores remains about 0.6 μm. HRTEM images revealed that the walls are composed of many 2.5-nm-diameter dark objects (Figs. 14.19a, b), which are contributed by single {$Mo_{72}Fe_{30}$} clusters. This result confirms that the {$Mo_{72}Fe_{30}$} clusters play a critical role in constructing the uniform honeycomb structures, together with the surfactant. SEM images indicated small holes of highly ordered honeycomb films exist inside the 500-nm thick walls. When the concentration of DODMACl is higher than 4.0 mg mL^{-1} in $CHCl_3$ ($c_{DODMACl}$ = 6.73 mmolL^{-1}), the unique honeycomb structures are not observed any more, as shown in Fig. 14.19d.

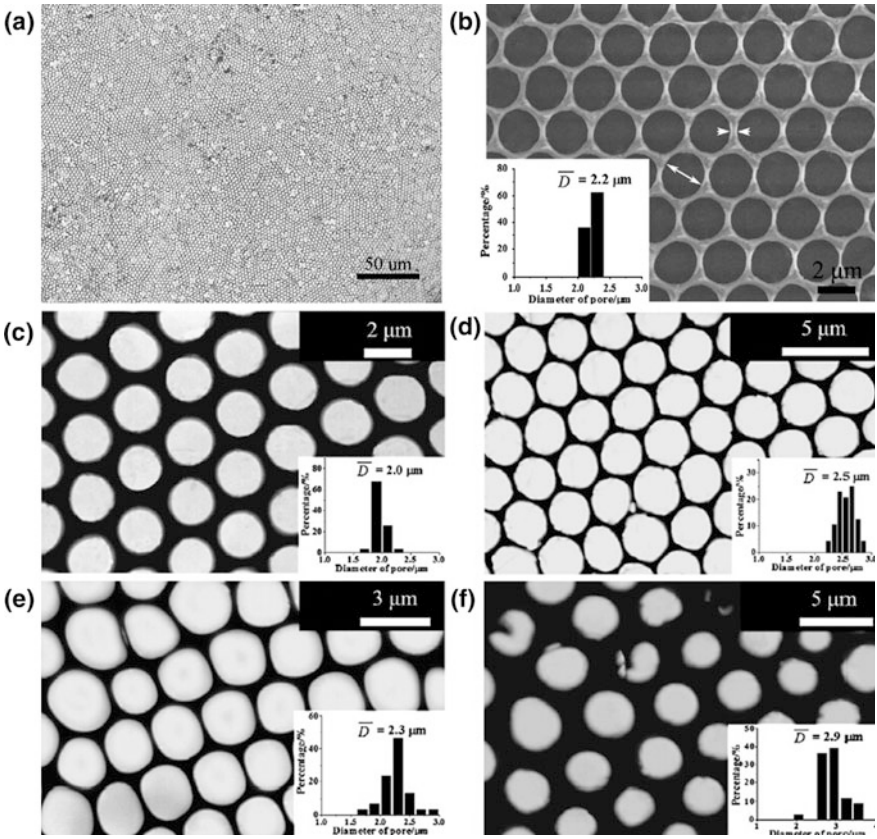

Fig. 14.20 **a** Optical microscope image (magnification ×400) of the porous honeycomb films of $DODMA^+$-encapsulated {$Mn_2Bi_2W_{20}$}. **b** SEM image. A pore and a wall are marked by the arrowheads. TEM images of the honeycomb films based on different $DODMA^+$-encapsulated polyoxometalates, including **c** ring-shaped {Mo_{154}} at $c_{DODMACl}$ = 2.6 mg mL^{-1}, **d** Keplerate spherical {Mo_{132}} at $c_{DODMACl}$ = 2.5 mg mL^{-1}, **e** hedgehog-shaped {Mo_{368}} at $c_{DODMACl}$ = 0.7 mg mL^{-1}, and **f** Keggin {PW_{12}} at $c_{(DODMA)3\{PW12\}}$ = 1.0 mg mL^{-1}. The insets show their pore size distribution. Reprinted from Ref. [81], Copyright 2011, with permission from Elsevier

Moreover, we fabricated highly ordered honeycomb-structured macroporous films by self-assembly of various surfactant-encapsulated polyoxometalates which have different compositions, shapes, and sizes, at the air/water interface without any extra moist airflow across the solution surface (Fig. 14.20) [81]. We choose a series of nanoscaled POMs with different shapes, sizes, and compositions, including $\{Mn_2Bi_2W_{20}\}$, $\{Mo_{154}\}$, $\{Mo_{132}\}$, $\{Mo_{368}\}$, and $\{PW_{12}\}$, to be the typical examples for inorganic cores. Based on the investigations of above POMs by our group, it can be concluded that, the self-assembly of surfactant-encapsulated POMs to the ordered macroporous honeycomb films at the air/water interface is a universal phenomenon, no matter with the compositions, shapes, and sizes of POMs.

14.3.2 Mechanism of Self-assembly of SECs into Honeycomb Films

How do polymers and/or HSECs self-assemble into ordered honeycomb films on solid substrates with a moist airflow and/or directly at the air/water interface? Although it should be very complicated, we are still trying to propose a resonable mechanism of the self-assembly at the air/water interface [82]. During the self-assembly, the rapid evaporation of organic solvent will debase the temperature around the solution surface. The water vapor around the solution surface will be condensed to become micrometer water droplets. These micrometer water droplets act as important templates for macropores, and the organic solvent concentrate and deposit around these water droplets [83, 84]. Meanwhile, the induced Marangoni convection [85] and local capillary forces mainly drive the water droplets to hexagonally arrange in a minimum energy state. After the complete evaporation of solvent, the surface will warm up. Thus the saturated water vapor pressure is increased, and the enveloped water droplet will be evaporated again. Consequently, pores are formed and materials are solidified in walls. The porous honeycomb films are finally obtained. In fact, the stability of the water droplets which are the

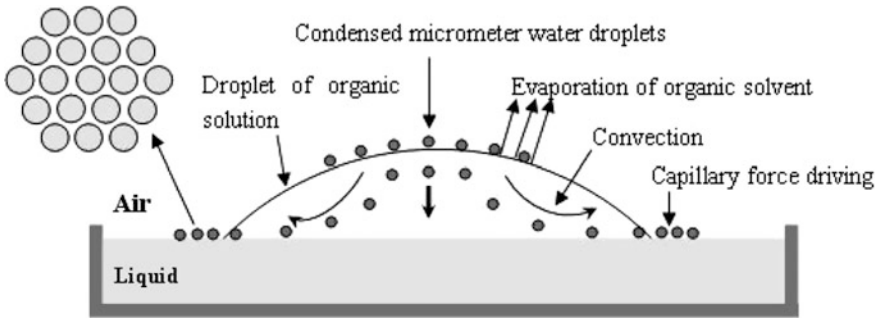

Fig. 14.21 The formation mechanism of periodic hexagonal honeycomb films at the air/water interface. Reprinted from Ref. [82], Copyright 2009, with permission from Elsevier

templates for honeycomb morphology is the crucial step (Fig. 14.21). Therefore, influences can be used to control the energy state of water droplets, and consequently, the morphology of the hybrid films can be modulated.

14.3.3 Morphology Modulation of Honeycomb Films of SECs

It can be speculated that the stabilization of micrometer water droplets is the crucial step during the self-assembly to porous honeycomb films. To further this hypothesis, we verified the honeycomb film morphology becomes changeable morphologies by modulating water droplet state.

Originally, we speculated that the fully hydrophobic complexes would spread homogeneously on the surface of water, similar to the case of spreading a layer of oil at the air/water interface. However, in reality we found that the arrangement of complexes was very complicated and dependent on surfactant concentration. As discussed in Sect. 14.3.1, an optimum surfactant concentration is fit for self-assembly into a honeycomb film. At lower or higher concentrations, no ordered honeycomb film is observed.

The surface properties of SECs, such as the hydrophobicity and the surface coverage, are also very importance in forming ordered honeycomb nanostructures. We chose three cation surfactants with different hydrophobic tails to encapsulate the $\{Mn_2Bi_2W_{20}\}$, resulting in the formation of $(DODMA)_{10}\{Mn_2Bi_2W_{20}\}$, $(DDDMA)_{10}\{Mn_2Bi_2W_{20}\}$ and $(CTA)_{10}\{Mn_2Bi_2W_{20}\}$ complex. Both $(DODMA)_{10}\{Mn_2Bi_2W_{20}\}$ and $(DDDMA)_{10}\{Mn_2Bi_2W_{20}\}$ can self-assemble into relatively ordered porous films at the air/water interface at the same amount of $\{Mn_2Bi_2W_{20}\}$, while for $(CTA)_{10}\{Mn_2Bi_2W_{20}\}$, there only formed less ordered fragment of complexes (Fig. 14.22). Furthermore, the hydrophobicity of SECs mainly lies in the surfactant chains and the surface coverage degree of polyoxometalates by encapsulating surfactants. Their hydrophilic lipophilic balance (HLB) values of surfactants and the surface coverage degree of polyoxometalates by surfactants in SECs which is equal to the percentage of surfactant volume to SECs volume are approximately calculated (Table 14.2). As we know, the smaller HLB value is, the stronger the hydrophobic of surfactants is. So the DODMA is more hydrophobic and has a larger surface coverage, DDDMA comes second. Therefore, we infer that hydrophobicity of the three complex is $(DODMA)_{10}\{Mn_2Bi_2W_{20}\} > (DDDMA)_{10}\{Mn_2Bi_2W_{20}\} > (CTA)_{10}\{Mn_2Bi_2W_{20}\}$. For the $(DODMA)_{10}\{Mn_2Bi_2W_{20}\}$ complex, the condensed water droplets can be well stabilized and form two dimensional microcosmic w/o structures, and finally, an ordered honeycomb film is self-organized at the air/water interface. However, the weak hydrophobicity and lower surface coverage cannot well stabilize the water droplets, so that no porous structure is obtained for $(CTA)_{10}\{Mn_2Bi_2W_{20}\}$ at the air/water interface. Therefore, it can be concluded that a higher hydrophobicity and lager surface coverage are beneficial to the self-assembly

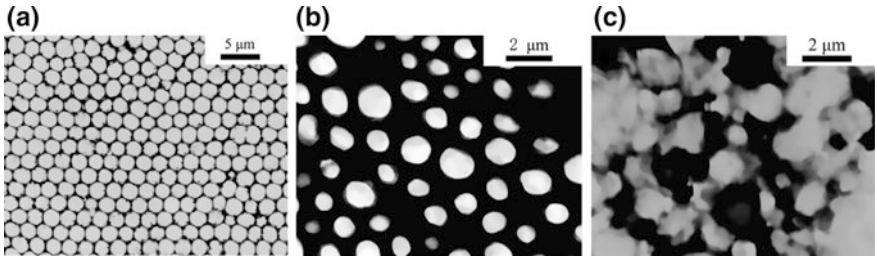

Fig. 14.22 TEM images of honeybomb films by casting three chloroform solutions at the air/water interface: **a** 1.7 mg mL^{-1} $(DODMA)_{10}\{Mn_2Bi_2W_{20}\}$; **b** 1.5 mg mL^{-1} $(DDDMA)_{10}\{Mn_2Bi_2W_{20}\}$; and **c** 1.3 mg mL^{-1} $(CTA)_{10}\{Mn_2Bi_2W_{20}\}$. Reprinted from Ref. [82], Copyright 2009, with permission from Elsevier

Table 14.2 The properties of the three cationic surfactants and the surface coverage of $\{Mn_2Bi_2W_{20}\}$ by surfactants (a is a constant)

Cationic surfactants	$DODMA^+$	$DDDMA^+$	CTA^+
HLB values	a-17.1	a-11.4	a-7.6
Volume of hydrophobic chains (nm^3)	1.02	0.70	0.46
Surface coverage of POM in SECs (%)	79	72	63

of honeycomb film at the air/water interface. Moreover, the air/solution interface not only provides a flat medium for preparing honeycomb films, but also the surface current of the supporting solutions can influence the morphologies of the obtained films.

In addition, the evaporation rate of solvents is another important factor during the process of self-assembly [82]. It is found that both carbon disulfide and chloroform solution of $(DODMA)_{10}\{Mn_2Bi_2W_{20}\}$ can form highly ordered honeycomb films at the air/water interface (Figs. 14.23a, b), with a pore size of $\sim$1 μm for carbon disulfide as the solvent and $\sim$2 μm taking chloroform as the solvent. Taking the boiling points of carbon disulfide and chloroform being 46 and 61 °C, respectively into account, it is easy to conclude that the higher the boiling point of the solvents is, the larger the pore sizes of the honeycomb films are. We presume that the condensed water droplets have more time to coalesce and grow during the self-organization if the boiling point of solvent is high. Consequently, the pores templated by water droplets are much larger. However, if the boiling points of solvents are too high, such as cyclohexane and n-heptane with the boiling points of 81 and 98 °C, respectively, it is also shown that no porous architectures are observed (Figs. 14.23c, d). It is because that solvent volatility is too slow to produce a sufficient temperature gradient around the organic solution surface; thus there are not enough condensed micrometer water droplets to template the formation of pores.

We also found that supporting solutions can influence the morphologies of the obtained films. The honeycomb porous film with a few disorderly arranged pores at

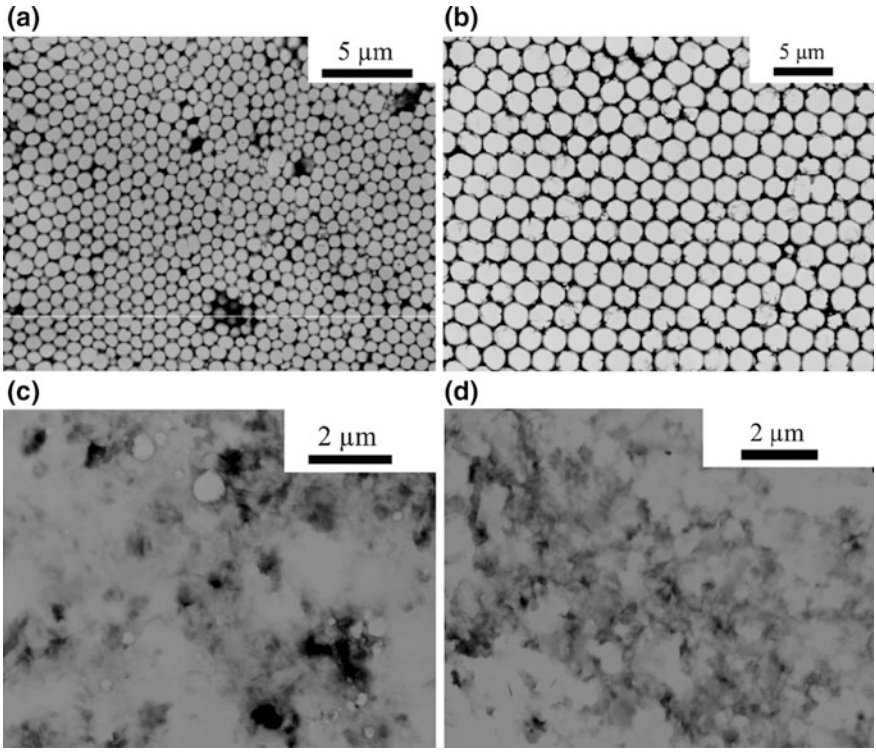

Fig. 14.23 TEM images of the honeycomb films prepared by dropping 1.7 mg mL^{-1} $(DODMA)_{10}\{Mn_2Bi_2W_{20}\}$ solution at the air/water interface by using different solvents: **a** carbon disulfide, **b** chloroform, **c** cyclohexane, and **d** *n*-heptane, respectively. Reprinted from Ref. [82], Copyright 2009, with permission from Elsevier

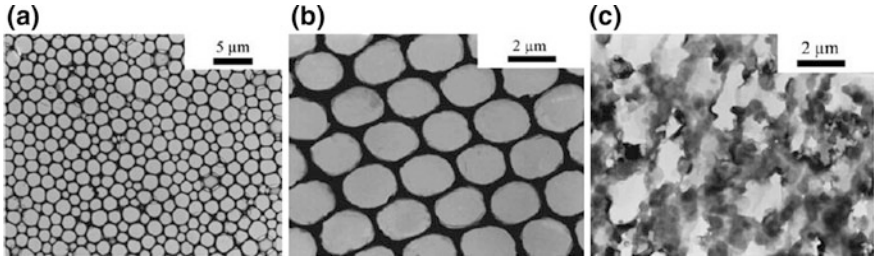

Fig. 14.24 TEM images of the thin films of $DODMA^+$-encapsulated $\{Mn_2Bi_2W_{20}\}$ at c_{DODMA+} = 1.0 mg mL^{-1} fabricated at the **a** air/water, **b** air/1 mol L^{-1} NaCl solution, and **c** air/2 mmol L^{-1} TTAB solution interfaces. Reprinted from Ref. [82], Copyright 2009, with permission from Elsevier

the air/water interface is fabricated by the $DODMA^+$ at c_{DODMA+} = 1.0 mg mL^{-1} and $\{Mn_2Bi_2W_{20}\}^{10-}$ at $c_{\{Mn2Bi2W20\}}$ = 1.0 mg mL^{-1}, which are shown in Fig. 14.24a. The same chloroform solution can self-assemble into a more close-packed hexagonal porous film by changing the supporting solution to the air/1 mol L^{-1} NaCl solution interface, shown in Fig. 14.24b. However, if 2 mmol L^{-1} TTAB solution acts as the supporting solution, because of their amphiphilicity, the surface tension can be reduced and cause a strong interfacial turbulence. Consequently, thin films with very disordered fragments without pores are observed (Fig. 14.24c). It can be concluded that the air/solution interface not only provides a flat medium for preparing honeycomb films, but also can influence the morphologies of the obtained films.

14.3.4 Excellent Properties of Honeycomb Films of SECs

As discussed above in Sect. 14.2, the nano-scale POM clusters are versatile, including magnetic properties, electrochem87ical properties and photoluminescent.

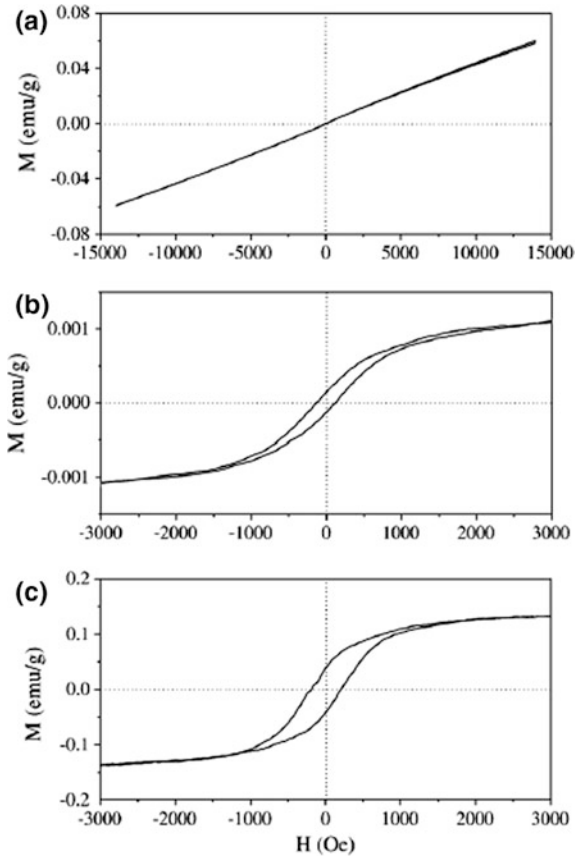

Fig. 14.25 Magnetic hysteresis loops of **a** $\{Mn_2Bi_2W_{20}\}$ crystals, **b** $(DODMA)_{10}\{Mn_2Bi_2W_{20}\}$ complexes, and **c** the ordered porous honeycomb film of $DODMA^+$-encapsulated $\{Mn_2Bi_2W_{20}\}$. Reprinted from Ref. [81], Copyright 2011, with permission from Elsevier

Combining the properties of POMs and the specificities of surfactants, hence, the self-assembled honeycomb films of surfactant encapsulated polyoxometalates could literally be described as a novel class of materials. Based on our investigations, it is found that $\{Mn_2Bi_2W_{20}\}$ crystals possess paramagnetism from the magnetic hysteresis loop, shown in Fig. 14.25 [81]. When the $\{Mn_2Bi_2W_{20}\}$ clusters are encapsulated by DODMA through electrostatic interaction, the formed $(DODMA)_{10}\{Mn_2Bi_2W_{20}\}$ complexes exhibit a little ferromagnetism (Fig. 14.25a). It can be calculated the coercive force (Hc) of 127 Oe and the residual magnetization/saturationmagnetization (Mr/Ms) of 0.12 (1.3×10^{-4} emu g^{-1}/ 1.1×10^{-3} emu g^{-1}) from the magnetic hysteresis loop (Fig. 14.25b), Further, the ordered honeycomb film of $DODMA^+$-encapsulated $\{Mn_2Bi_2W_2\}$ self-assembled at the air/water interface by $(DODMA)_{10}\{Mn_2Bi_2W_{20}\}$ complexes magically possesses a stronger ferromagnetism with Hc of 193 Oe and Mr/Ms of 0.27 (0.037 emu g^{-1}/ 0.137 emu g^{-1}) which may due to the synergistic effect of the POMs and surfactants.

In addition, ordered honeycomb films of SECs exhibit excellent electrochemical properties. As an example, the electrochemical properties of the ordered honeycomb film of $DODMA^+$-encapsulated $\{Mo_{368}\}$ is studied by using a cyclic voltammetry (CV) method, and the reference electrode, counter electrode and electrolyte solution are saturated calomel electrode, platinum sheet and 0.5 mol L^{-1} H_2SO_4 soultion, respectively. The honeycomb film of $DODMA^+$-encapsulated $\{Mo_{368}\}$ was transferred onto the ITO-glass which used as the working electrode, and then the bare region was carefully covered by the insulating nail polish in order to precisely detect the honeycomb film-coated electrode surface. Compared with the dotted lines which indicate that no active species are behaved for bare ITO and DODMACl in 0.5 mol L^{-1} H_2SO_4 solution. Comparing the cyclic voltammetry of $\{Mo_{368}\}$ and the honeycomb film (as shown in Fig. 14.26, solid line), one can speculate that the electrochemical properties of the honeycomb film of $DODMA^+$-encapsulated $\{Mo_{368}\}$ are derived from the inorganic $\{Mo_{368}\}$. However, the changes may be ascribed to the electrostatic interaction of POMs and surfactants.

Due to the intrinsic fluorescence of the europium polyoxometalate anion, $[EuW_{10}O_{36}]^{9-}$, the porous honeycomb films of $(DODMA)_9[EuW_{10}O_{36}]$ complexes can emit fluorescence when they are excited by UV light, presenting excelent photoluminescent property [86]. In the polyoxometalate structure of $Na_9[EuW_{10}O_{36}]\cdot 32H_2O$, Eu^{3+} is located in the center of $[EuW_{10}O_{36}]$, which achieves 8-fold coordination by the attachment of twoW_5O_{18} ligands, forming a distorted square antiprism. The photo excitation of the O → W charge transfer (CT) of $[EuW_{10}O_{36}]$ induces the emission of Eu^{3+}. When the UV light at a wavelength of 270 nm irradiated the honeycomb film, the luminescence derived from the $^5D_0 \rightarrow {}^7F_J$ (J ≈ 1, 2, 3, and 4) transition can be observed. As shown in Fig. 14.27c (black curve), the emission band of $[EuW_{10}O_{36}]$ crystals at 593 nm corresponds to the $^5D_0 \rightarrow {}^7F_1$ emission transition. A strong band at 619 nm is attributed to the $^5D_0 \rightarrow {}^7F_2$ emission transition. The much less intense bands at 650 and 698 nm are assigned to the$^5D_0 \rightarrow {}^7F_3$ and $^5D_0 \rightarrow {}^7F_4$ emission transitions, respectively. The weak emission peak at 580 nm in $[EuW_{10}O_{36}]$ crystals disappears when the $(DODMA)_9[EuW_{10}O_{36}]$ complexes formed, and the relative intensities

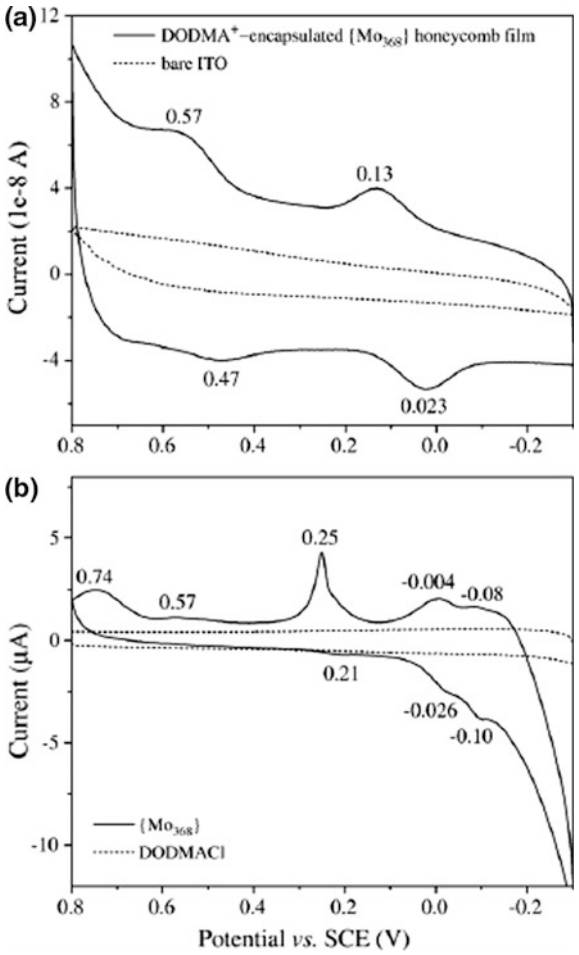

Fig. 14.26 Cyclic voltammograms of **a** the honeycomb film of $DODMA^+$-encapsulated $\{Mo_{368}\}$ (*solid line*) and bare ITO (*dotted line*), **b** $\{Mo_{368}\}$ (*solid line*) and DODMACl (*dotted line*). All the curves were measured in 0.5 mol L^{-1} H_2SO_4 solution. Scan rate 50 mV s^{-1}. Reprinted from Ref. [81], Copyright 2011, with permission from Elsevier

and the band widths are also a little changed, which may be attributed to the change of the Eu^{3+} microenvironment in $(DODMA)_9[EuW_{10}O_{36}]$ complexes.

In order to broaden applications of the honeycomb porous films, the surfactant encapsulated POMs honeycomb films used as templates to directionally electrodeposit gold nanoparticles into their macropores also have been investigated [87]. As shown in Figs. 14.28a, Au nanoparticles are well-deposited into the honeycomb pores but not on the walls. It is reasonable according to the formation mechanism of honeycomb films discussed in the Sect. 14.3.2. After transferring the honeycomb films of $(DODMA)_{10}\{Mn_2Bi_2W_{20}\}$ onto ITO-coated glass, the holes are the bare ITO conductive surface, which can provide channels for electron transfer onto the working electrode. However, the electro-deposition is prevented owing to the insulation of DODMA. Consequently, Au nanoparticles prefer to electro-deposit into the macropores rather than the walls. Rhodamine 6G (R6G) is a

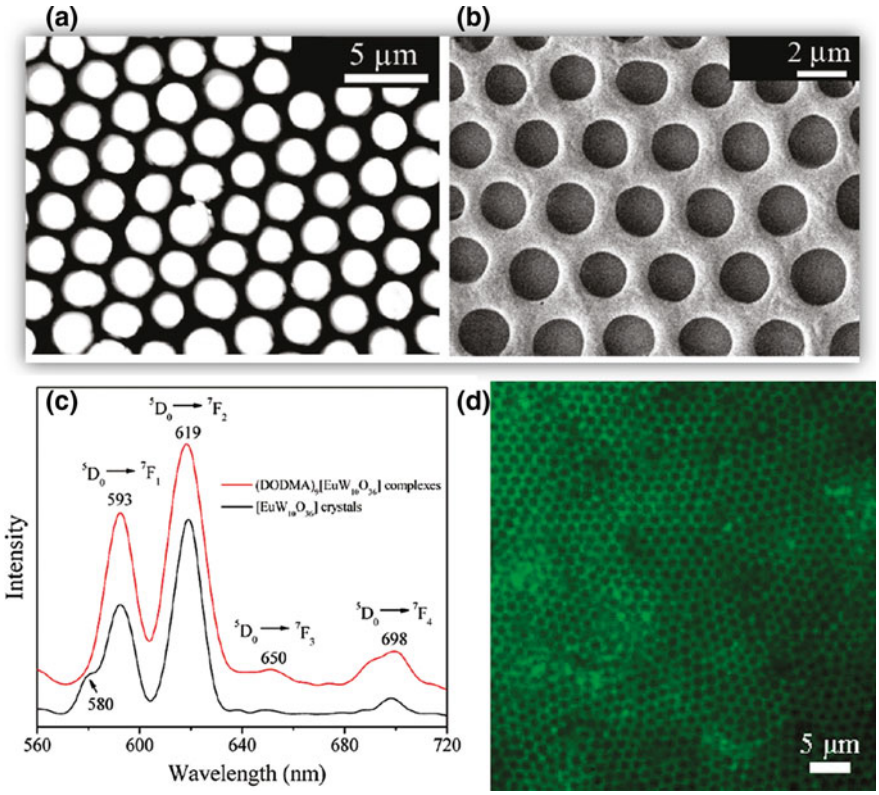

Fig. 14.27 Micrograph images of self-assembled honeycomb films of $(DODMA)_9[EuW_{10}O_{36}]$ complexes at the air/water interface. **a** TEM image. **b** SEM image. **c** Fluorescence spectra of an aqueous solution of $[EuW_{10}O_{36}]$ crystals (*black curve*) and a chloroform solution of $(DODMA)_9[EuW_{10}O_{36}]$ complexes (*red curve*), excited at 270 nm. The positions of $^5D_0 \rightarrow {}^7F_J$ ($J \approx 1, 2, 3$, and 4) emission bands are indicated. **d** Typical fluorescence micrograph of the porous honeycomb film of $(DODMA)_9[EuW_{10}O_{36}]$ complexes, which is irradiated by a mercury lamp. Reprinted with permission from Ref. [86]. Copyright 2010 by American Physical Society

strongly fluorescent xanthene derivative, which can be used as a model to evaluate the enhanced Raman scattering signal of organic molecules by honeycomb films. In Fig. 14.28b, no Raman signal for R6G was detected for bare ITO-coated glass (curve 1). Coincidentally, R6G was not detected for the honeycomb film-covered ITO-coated glass because of the coverage of the honeycomb films, it was also difficult to detect the glass vibrations. Interestingly, R6G signals were obviously detected for directly electrodeposited Au nanoparticles (curve 3) and Au-filled honeycomb films (curve 4). In particular, curve 4 presents a much stronger SERS effect, which may be due to the hierarchical structure of the microscaled array and nanoscaled particles. The results indicate that the hierarchical Au-filled honeycomb film is a good detector of R6G molecules.

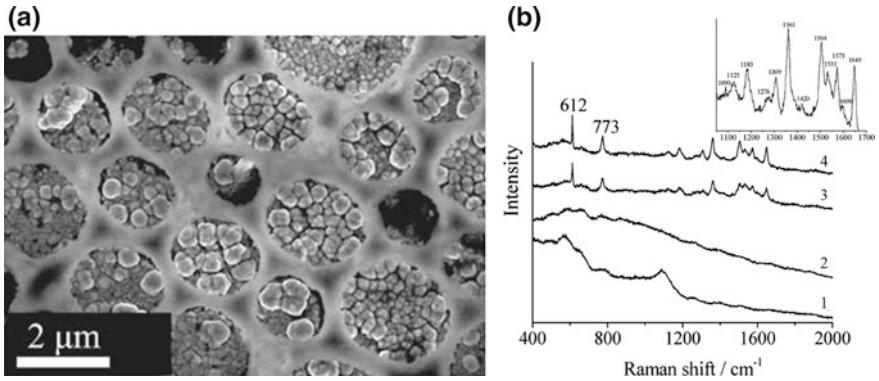

Fig. 14.28 **a** SEM image of the hierarchical array with Au nanoparticles directionally electrodeposited into the honeycomb macropores. **b** Raman scattering spectra of R6G on (1) the bare ITO-coated glass, (2) the honeycomb film-covered ITO-coated glass and (3, 4) the Au-deposited ITO-coated glass. The Au nanoparticles were electrodeposited without the honeycomb film template in (3) and with the honeycomb film template in (4). The honeycomb film template was dissolved in chloroform before Raman preparation for sample D. The inset shows the magnification of curve d from 1050 to 1700 cm^{-1}. The Raman measurements were all conducted using an excitation wavelength of 532 nm and with a 20 s accumulation. Reproduced from Ref. [87] by permission of The Royal Society of Chemistry (RSC) on behalf of the Centre National de la Recherche Scientifique (CNRS) and the RSC

14.3.5 Conclusion

Nano-scale polyoxometalates (POMs) are a class of discrete anionic metal oxides that can be viewed as transferable building blocks, which can be applied in the preparation of functional materials. The past decades have witnessed the significant advancement in the synthesis and application of POMs-based materials. More amazingly, based on their excellent water solubility, according to electrostatic interactions, these inorganic macroions demonstrate some features that usually are believed to belong only to complex biological molecules, such as the self-recognition in dilute solutions. Meanwhile, polyoxometalates-based organic-inorganic hybrid materials possess amphiphilic properties by self-assembling into supramolecular architectures, e.g. vesicles, reverse vesicles or onionlike structures in polar and non-polar solvents. Moreover, self-assembly of surfactant-encapsulated POM clusters into honeycomb films at the air/water interface, which is templated by condensed water micro-droplets are functionally attractive. So far, only a few interesting properties of amphiphilic hybrid POMs have been studied. There are still challenges and much more exploration is necessary in the development of POMs. Many efforts have been made to comprehensively understand fascinate chemical and physical properties of POMs and to design rational synthetic strategies and synthesize novel amphiphilic hybrid POMs. We believe that a better understanding of mechanism will no doubt help in judicious design and improve the function of highly efficient POM-based materials. In addition, the basic investigations of the structure and

assembly of POMs, organic-inorganic hybrids of multilayer films and porous films containing POMs are also worthy of thorough investigation for applications in catalysis, medicine, smart materials, and beyond will open new vistas in materials research and build a bridge between polyoxometalate chemistry and material chemistry.

References

1. Pope MT, Müller A (1991) Polyoxometalate chemistry: an old field with new dimensions in several disciplines. Angew Chem Int Ed Engl 30:34–48
2. Pope MT (1983) Heteropoly and isopoly oxometalates. Springer, Berlin
3. Rao CNR, Müller A, Cheetham AK (Eds) (2006) The chemistry of nanomaterials: synthesis, properties and applications. Wiley, New York
4. Gouzerh P, Proust A (1998) Main-group element, organic, and organometallic derivatives of polyoxometalates. Chem Rev 98:77–112
5. Weinstock IA (1998) Homogeneous-phase electron-transfer reactions of polyoxometalates. Chem Rev 98:113–170
6. Müller A, Peters F, Pope MT, Gatteschi D (1998) Polyoxometalates: very large clusters nanoscale magnets. Chem Rev 98:239–272
7. Mizuno N, Kamata K (2011) Catalytic oxidation of hydrocarbons with hydrogen peroxide by vanadium-based polyoxometalates. Coord Chem Rev 255:2358–2370
8. Hill CL (2007) Special issue: polyoxometalates in catalysis-foreword. J Mol Catal A: Chem 262:1–1
9. Rhule JT, Hill CL, Judd DA, Schinazi RF (1998) Polyoxometalates in medicine. Chem Rev 98:327–358
10. Hasenknopf B (2005) Polyoxometalates: introduction to a class of inorganic compounds and their biomedical applications. Front Biosci 10:275
11. Long DL, Burkholder E, Cronin L (2007) Polyoxometalate clusters, nanostructures and materials: from self-assembly to designer materials and devices. Chem Soc Rev 36:105–121
12. Kim KC, Pope MT (1999) Cation-directed structure changes in polyoxometalate chemistry. equilibria between isomers of bis (9-tungstophosphatodioxouranate (VI)) complexes. J Am Chem Soc 121:8512–8517
13. Briot E, Piquemal JY, Vennat M, Brégeault JM, Chottard G, Manoli JM (2000) Aqueous acidic hydrogen peroxide as an efficient medium for tungsten insertion into MCM-41 mesoporous molecular sieves with high metal dispersion. J Mater Chem 10:953–958
14. Zhai QG, Wu XY, Chen SM, Zhao ZG, Lu CG (2007) Construction of Ag/1, 2, 4-triazole/polyoxometalates hybrid family varying from diverse supramolecular assemblies to 3-D rod-packing framework. Inorg Chem 46:5046–5058
15. Landsmann S, Luka M, Polarz S (2012) Bolaform surfactants with polyoxometalate head groups and their assembly into ultra-small monolayer membrane vesicles. Nat Commun 3:1299
16. Izzet G, Abécassis B, Brouri D, Piot M, Matt B, Serapian SA, Bo C, Proust A (2016) Hierarchical self-assembly of polyoxometalate-based hybrids driven by metal coordination and electrostatic interactions: from discrete supramolecular species to dense monodisperse nanoparticles. J Am Chem Soc 138:5093–5099
17. Liu H, Hsu CH, Lin ZW, Shan WP, Wang J, Jiang J, Huang MJ, Lotz B, Yu XF, Zhang WB, Yue K, Cheng SZD (2014) Two-dimensional nanocrystals of molecular janus particles. J Am Chem Soc 136:10691–10699
18. Sun HG, Tu YF, Wang CL, Van Horn RM, Tsai CC, Graham MJ, Sun B, Lotz B, Zhang WB, Cheng SZD (2011) Hierarchical structure and polymorphism of a sphere-cubic shape

amphiphile based on a polyhedral oligomeric silsesquioxane-[60] fullerene conjugate. J Mater Chem 21:14240–14247
19. Keggin JF (1934) Structure and formula of 12-phosphotungstic acid. Proc R Soc A 144:75–79
20. Dawson B (1953) The structure of the 9 (18)-heteropoly anion in potassium 9 (18)-tungstophosphate, K_6 $(P_2W_{18}O_{62})\cdot 14H_2O$. Acta Cryst 6:113–126
21. Waugh JCT, Schoemaker DP, Pauling L (1954) On the structure of the heteropoly anion in ammonium 9-molybdomanganate, $(NH_4)_6MnMo_9O_{32}\cdot 8H_2O$. Acta Cryst 7:438–441
22. Anderson JS (1937) Constitution of the poly-acids. Nature 140:850–851
23. Tsay YH, Silverton JVZ (1973) Krist 137:256
24. Lindquist I (1950) A crystal structure investigation of the paramolybdate ion. Ark Kemi 2:325–341
25. Müller A, Beckmann E, Bögge H, Schmidtmann M, Dress A (2002) Inorganic chemistry goes protein size: a Mo368 nano-hedgehog initiating nanochemistry by symmetry breaking. Angew Chem Int Ed 41:1162–1167
26. Bösing M, Nöh A, Loose I, Krebs B (1998) Highly efficient catalysts in directed oxygen-transfer processes: synthesis, structures of novel manganese-containing heteropolyanions, and applications in regioselective epoxidation of dienes with hydrogen peroxide. J Am Chem Soc 120:7252–7259
27. Sugeta M, Yamase T (1993) Crystal structure and luminescence site of Na_9 $(EuW_{10}O_{36})\cdot 32H_2O$. Bull Chem Soc Jpn 66:444–449
28. Müller A, Das SK, Fedin VP, Krickemeyer E, Beugholt C, Bögge H, Schmidtmann M, Hauptfleisch B (1999) Rapid and simple isolation of the crystalline molybdenum-blue compounds with discrete and linked nanosized ring-shaped anions: Na_{15} $[Mo_{\{126\}}\{VI\}Mo_{\{28\}}VO_{462}H_{14}(H_2O)_{70}]_{0.5}[Mo_{\{124\}}\{VI\}Mo_{\{28\}}VO_{457}H_{14}(H_2O)_{68}]$ $0.5\cdot$ca.$400H_2O$ and Na_{22} $[Mo_{\{118\}}\{VI\}Mo_{\{28\}}VO_{442}H_{14}(H_2O)_{58}]\cdot$ca.$250H_2O$. Z Anorg Allg Chem 625:1187–1192
29. Müler A, Krickemeyer E, Bögge H, Schmidtmann M, Peters F (1998) Organizational forms of matter: an inorganic super fullerene and keplerate based on molybdenum oxide. Angew Chem Int Ed 37:3359–3363
30. Müller A, Sarkar S, Shah SQN, Bögge H, Schmidtmann M, Sarkar S, Kögerler P, Hauptfleisch B, Trautwein AX, Schünemann V (1999) Archimedean synthesis and magicnumbers: "sizing" giant molybdenum-oxide-based molecular spheres of the keplerate type. Angew Chem Int Ed 38:3238–3241
31. Botar B, Kogerler P, Hill CL (2005) $[\{(Mo)Mo_5O_{21}(H_2O)_3(SO_4)\}_{12}(VO)_{30}(H_2O)_{20}]^{36-}$: a molecular quantum spin icosidodecahedron. Chem Commun 25:3138–3140
32. Howell RC, Perez FG, Jain S, Horrocks JWD, Rheingold AL, Francesconi LC (2001) A new type of heteropolyoxometalates formed from lacunary polyoxotungstate ions and europium or yttrium cations. Angew Chem Int Ed 113:4155–4158
33. Mal SS, Kortz U (2005) The wheel-shaped Cu_{20} Tungstophosphate $[Cu_{20}Cl(OH)_{24}(H_2O)_{12}(P_8W_{48}O_{184})]_{25}$-Ion. Angew Chem Int Ed 44:3777–3780
34. Todea AM, Merca A, Bögge H, Slageren J, Dressel M, Engelhardt L, Luban M, Glaser T, Henry M, Müller A (2007) Extending the (Mo)Mo5}12M30 capsule keplerate sequence: A {Cr30 cluster of s = 3/2 metal centers with a Na(H2O)12 encapsulate. Angew Chem Int Ed 46:6106–6110
35. Pichon C, Mialane P, Dolbecq A, Marrot J, Rivière E, Bassil BS, Kortz U, Keita B, Nadjo L, Sécheresse F (2008) Octa-and nonanuclear nickel (II) polyoxometalate clusters: synthesis and electrochemical and magnetic characterizations. Inorg Chem 47:11120–11128
36. Müller A, Luban M, Schröder C, Modler R, Kögerler P, Axenovich M, Schnack J, Canfield P, Bud'ko S, N N (2001) Classical and quantum magnetism in giant keplerate magnetic molecules. Chem Phys Chem 2:517–521
37. Lopez X, Maestre JM, Bo C, Poblet JM (2001) Electronic properties of polyoxometalates: A DFT study of α/β-$[XM_{12}O_{40}]$ n-relative stability (M = W, Mo and X a main group element). J Am Chem Soc 123:9571–9576

38. Jabbour D, Keita B, Nadjo L, Kortz U, Mal SS (2005) The wheel-shaped Cu_{20}-tungstophosphate $[Cu_{20}Cl(OH_{24}(H_2O)_{12}(P_8W_{48}O_{184})^{25-}$, redox and electrocatalytic properties. Electrochem Commun 7:841–847
39. Keita B, Zhang G, Dolbecq A, Mialane P, Sécheresse F, Miserque F, Nadjo L (2007) MoV-MoVI Mixed valence polyoxometalates for facile synthesis of stabilized metal nanoparticles: Electrocatalytic oxidation of alcohols. J Phys Chem C 111:8145–8148
40. Mbomekalle IM, Keita B, Lu YW, Nadjo L, Contant R, Belai N, Pope MT (2004) Synthesis, characterization and electrochemistry of the novel Dawson-type tungstophosphate $[H_4PW_{18}O_{62}]^{7-}$ and first transition metal ions derivatives. Eur J Inorg Chem 2004:276–285
41. Liu TB, Imber B, Diemann E, Liu G, Cokleski K, Li HL, Chen ZQ, Müller A (2006) Deprotonations and charges of well-defined Mo72Fe30 nanoacids simply stepwise tuned by pH allow control/variation of related self-assembly processes. J Am Chem Soc 128:15914–15920
42. Kistler ML, Liu TB, Gouzerh P, Todea AM, Müller AM (2009) Molybdenum-oxide based unique polyprotic nanoacids showing different deprotonations and related assembly processes in solution. Dalton Trans 26:5094–5100
43. Todea AM, Merca A, Bögge H, Glaser T, Pigga JM, Langston MLK, Liu T, Prozorov R, Luban M, Schröder C, Casey WH, Müller A (2010) Porous capsules $\{(M)\ M_5\}_{12}FeIII_{30}$ ($M = Mo^{VI}$, W^{VI}): sphere surface supramolecular chemistry with 20 ammonium ions, related solution properties, and tuning of magnetic exchange interactions. Angew Chem Int Ed 49:514–519
44. Kistler ML, Patel KG, Liu TB (2009) Accurately tuning the charge on giant polyoxometalate type keplerates through stoichiometric interaction with cationic surfactants. Langmuir 25:7328–7334
45. Wang Y, Li H, Qi W, Yang Y, Yan Y, Li B, Wu LX (2012) Supramolecular assembly of chiral polyoxometalate complexes for asymmetric catalytic oxidation of thioethers. J Mater Chem 22:9181–9188
46. Lee IS, Long JR, Prusiner SB, Safar JG (2005) Selective precipitation of prions by polyoxometalate complexes. J Am Chem Soc 127:13802–13803
47. Geng J, Li M, Ren JS, Wang EB, Qu XG (2011) Polyoxometalates as inhibitors of the aggregation of amyloid β peptides associated with Alzheimer's disease. Angew Chem Int Ed 50:4184–4188
48. Geng J, Li M, Ren JS, Wang EB, Qu XG (2011) Polyoxometalates as inhibitors of the aggregation of amyloid β peptides associated with Alzheimer's disease. Angew Chem 123:4270–4274
49. Yan XH, Zhu PL, Fei JB, Li JB (2010) Self-assembly of peptide-inorganic hybrid spheres for adaptive encapsulation of guests. Adv Mater 22:1283–1287
50. Goovaerts V, Stroobants K, Absillis G, Parac-Vogt TN (2013) Molecular interactions between serum albumin proteins and Keggin type polyoxometalates studied using luminescence spectroscopy. Phys Chem Chem Phys 15:18378–18387
51. Kosik KS (1992) Alzheimer's disease: a cell biological perspective. Science 256:780–783
52. Yamin G, Ono K, Inayathullah M, Teplow DB (2008) Amyloid β-protein assembly as a therapeutic target of Alzheimer's disease. Curr Pharm Des 14:3231–3246
53. Gao N, Sun H, Dong K, Ren J, Duan T, Xu C, Qu XG (2014) Transition-metal-substituted polyoxometalate derivatives as functional anti-amyloid agents for Alzheimer's disease. Nat Commun 5:3422
54. Li M, Xu C, Wu L, Ren J, Wang E, Qu XG (2013) Self-assembled peptide-polyoxometalate hybrid nanospheres: two in one enhances targeted inhibition of amyloid β-peptide aggregation associated with Alzheimer's disease. Small 9:3455–3461
55. Li J, Chen Z, Zhou M, Jing J, Li W, Wang Y, Wu L, Wang L, Wang Y, Lee M (2016) Polyoxometalate-driven self-assembly of short peptides into multivalent nanofibers with enhanced antibacterial activity. Angew Chem Int Ed 55:2592–2595

56. Xu J, Zhao S, Han Z, Wang X, Song YF (2011) Layer-by-layer assembly of Na_9 $[EuW_{10}O_{36}]\cdot 32H_2O$ and layered double hydroxides leading to ordered ultra-thin films: cooperative effect and orientation effect. Chem Eur J 17:10365–10371
57. Kurth DG, Lehmann P, Volkmer D, Cölfen H, Koop MJ, Müller A, Chesne AD (2000) Surfactant-encapsulated clusters (SECs): $(DODA)_{20}(NH_4)[H_3Mo_{57}V_6(NO)_6O_{183}(H_2O)_{18}]$, a case study. Chem Eur J 6:385–393
58. Caruso F, Kurth DG, Volkmer D, Koop MJ, Müller A (1998) Ultrathin molybdenum polyoxometalate-polyelectrolyte multilayer films. Langmuir 14:3462–3465
59. Iler RK (1966) Multilayers of colloidal particles. J Colloid Interface Sci 21:569–594
60. Niu P, Hao J (2011) Fabrication of titanium dioxide and tungstophosphate nanocomposite films and their photocatalytic degradation for methyl orange. Langmuir 27:13590–13597
61. Fan D, Hao J (2009) Fabrication and electrocatalytic properties of chitosan and Keplerate-type polyoxometalate $\{Mo_{72}Fe_{30}\}$ hybrid films. J Phys Chem B 113: 7513-7516
62. Han F, Kambala V, Srinivasan M, Rajarathnam D, Naidu R (2009) Tailored titanium dioxide photocatalysts for the degradation of organic dyes in wastewater treatment: a review. Appl Catal A 359:25–40
63. Niu P, Hao J (2012) Efficient degradation of methyl orange via multilayer films of titanium dioxide and silicotungstic acid. Sci China Chem 55:2366–2372
64. Niu P, Hao J (2014) Efficient degradation of organic dyes by titaniumdioxide–silicotungstic acid nanocomposite films: Influenceof inorganic salts and surfactants. Colloids Surf A 443:501–507
65. Niu P, Hao J (2013) Photocatalytic degradation of methyl orange by titanium dioxide-decatungstate nanocomposite films supported on glass slides. Colloids Surf A 431:127–132
66. Volkmer D, Chesne AD, Kurth DG, Schnablegger H, Lehmann P, Koop J, Müller A (2000) Toward nanodevices: synthesis and characterization of the nanoporous surfactant-encapsulated Keplerate $(DODA)_{40}(NH_4)_2[(H_2O)_n \subset Mo_{132}O_{372}(CH_3COO)_{30}(H_2O)_{72}]$. J Am Chem Soc 122:1995–1998
67. Zhang J, Song Y, Cronin L, Liu T (2008) Self-assembly of organic–inorganic hybrid amphiphilic surfactants with large polyoxometalates as polar head groups. J Am Chem Soc 130:14408–14409
68. Jia Y, Zhang J, Zhang Z, Li Q, Wang E (2014) Metal-centered polyoxometalates encapsulated by surfactant resulting in the thermotropic liquid crystal materials. Inorg Chem Commun 43:5–9
69. Li W, Wu L (2014) Liquid crystals from star-like clusto-supramolecular macromolecules. Polym Int 63:1750–1764
70. He Z, Ai H, Li B, Wu L (2012) A supramolecular gel based on an adenine symmetrically grafted Anderson-type polyoxometalate complex. Chin Sci Bull 57:4304–4309
71. Sun H, Yang Q, Hao J (2016) Self-patterning porous films of giant vesicles of $\{Mo_{72}Fe_{30}\}(DODMA)_3$ complexes as frameworks. Adv Colloid Interface Sci 235:14–22
72. Tanford C (1972) Micelle shape and size. J Phys Chem 76:3020–3024
73. Zhou SJ, Feng YQ, Chen MJ, Li Q, Liu BY, Cao JM, Sun XF, Li HG, Hao J (2016) Robust onionlike structures with magnetic and photodynamic properties formed by a fullerene C_{60}-POM hybrid. Chem Commun 52:12171–12174
74. Song A, Dong S, Jia X, Hao J, Liu W, Liu T (2005) An onion phase in salt-free zero-charged catanionic surfactant solutions. Angew Chem Int Ed 44:4018–4021
75. Dong R, Zhong Z, Hao J (2012) Self-assembly of onion-like vesicles induced by charge and rheological properties in anionic-nonionic surfactant solutions. Soft Matter 8:7812–7821
76. Widawski G, Rawiso M, Francois B (1994) Self-organized honeycomb morphology of star-polymer polystyrene films. Nature 369:387–389
77. Sun F, Cai W, Li Y, Cao B, Lei Y, Zhang L (2004) Morphology-controlled growth of large-area two-dimensional ordered pore arrays. Adv Funct Mater 14:283–288
78. Kulinowski KM, Jiang P, Vaswani H, Colvin VL (2000) Porous metals from colloidal templates. Adv Mater 12:833–838

79. Nishikawa T, Nishida J, Ookura R, Nishimura SI, Scheumann V, Zizlsperger M, Lawall R, Knoll W, Shimomura M (2000) Web-structured films of an amphiphilic polymer from water in oil emulsion: fabrication and characterization. Langmuir 16:1337–1342
80. Shimomura M, Sawadaishi T (2001) Bottom-up strategy of materials fabrication: a new trend in nanotechnology of soft materials. Curr Opin Colloid Interface Sci 6:11–16
81. Fan D, Jia X, Tang P, Hao J, Liu T (2007) Self-patterning of hydrophobic materials into highly ordered honeycomb nanostructures at the air/water interface. Angew Chem Int Ed 119:3406–3409
82. Tang P, Hao J (2011) Macroporous honeycomb films of surfactant-encapsulated polyoxometalates at air/water interface and their electrochemical properties. Adv Colloid Interface Sci 161:163–170
83. Tang P, Hao J (2009) Formation mechanism and morphology modulation of honeycomb hybrid films made of polyoxometalates/surfactants at the air/water interface. J Colloid Interface Sci 333:1–5
84. Pitois O, Francois B (1999) Crystallization of condensation droplets on a liquid surface. Colloid Polym Sci 277:574–578
85. Stenzel MH (2002) Formation of regular honeycomb-patterned porous film by self-organization. Aust J Chem 55:239–243
86. Block MJ (1956) Surface tension as the cause of Bénard cells and surface deformation in a liquid film. Nature 178:650–651
87. Tang P, Hao J (2010) Photoluminescent honeycomb films templated by microwater droplets. Langmuir 26:3843–3847
88. Tang P, Hao J (2010) Directionally electrodeposited gold nanoparticles into honeycomb macropores and their surface-enhanced Raman scattering. New J Chem 34:1059–1062